



UNIVERSITY OF THESSALY  
DEPARTMENT OF MECHANICAL ENGINEERING

Diploma Thesis

**3D Microstructure Reconstruction of a HP-Nb Reformer Tube  
Exposed at Elevated Temperature Service**

Author: Nikolaos Korfiatis

Supervisor: Dr. Anna Zervaki

Volos, October 2019

© 2019 Κορφιάτης Νικόλαος

Η έγκριση της διπλωματικής εργασίας από το Τμήμα Μηχανολόγων Μηχανικών της Πολυτεχνικής Σχολής του Πανεπιστημίου Θεσσαλίας δεν υποδηλώνει αποδοχή των απόψεων του συγγραφέα (Ν. 5343/32 αρ. 202 παρ. 2)

### **Εγκρίθηκε από τα Μέλη της Τριμελούς Εξεταστικής Επιτροπής:**

Πρώτος Εξεταστής  
(Επιβλέπων)

Δρ. Άννα Ζερβάκη  
Εργαστηριακό Διδακτικό Προσωπικό  
Τμήμα Μηχανολόγων Μηχανικών  
Πανεπιστήμιο Θεσσαλίας

Δεύτερος Εξεταστής

Δρ. Κωνσταντίνος Παπαδημητρίου  
Καθηγητής  
Τμήμα Μηχανολόγων Μηχανικών  
Πανεπιστήμιο Θεσσαλίας

Τρίτος Εξεταστής

Δρ. Χαραλάμπους Γεώργιος  
Επίκουρος Καθηγητής  
Τμήμα Μηχανολόγων Μηχανικών  
Πανεπιστήμιο Θεσσαλίας

## Acknowledgements

Αρχικά θα ήθελα να ευχαριστήσω την επιβλέπουσα της διπλωματικής αυτής εργασίας, Δρ. Άννα Ζερβάκη. Όχι μόνο για την καθοριστική συμβολή στην εργασία αυτή και ιδιαίτερα στην συγγραφή της, αλλά και για την υπέροχη ευκαιρία που από κοινού με τον Δρ. Γρηγόριο Χαϊδεμενόπουλο μου έδωσαν, να βρεθώ σαν βοηθός στις εργαστηριακές τους μελέτες, καθώς επίσης και να παρουσιάσουμε μέρος της εργασίας στο EUROMAT 2019. Θεωρώ ίσως πιο σημαντικό από όλα να αναφέρω πόσο σημαντικό είναι ένας νέος με όρεξη, πίστη, θέληση και φιλότιμο να δέχεται μια όμορφη ευκαιρία από σπουδαίους ανθρώπους.

Ακόμη θα ήθελα να ευχαριστήσω τους καθηγητές Κ.Κ. Κωνσταντίνο Παπαδημητρίου και Γιώργο Χαραλάμπους για τον χρόνο που διέθεσαν στην εξέταση και αξιολόγηση της εργασίας. Αξιοσημείωτη είναι επίσης η συνεισφορά της καθηγήτριας του Α.Π.Θ. Κα. Ελένης Παυλίδου στην διεξαγωγή χημικών αναλύσεων στο SEM καθώς και του καθηγητή στην Σ.Σ.Ε. Κ. Διονύσιου Μουζάκη.

Επίσης θα ήθελα να αφιερώσω την εργασία αυτή στην ομάδα Κένταυρος, εφόσον από εκεί ξεκίνησε ένα όμορφο ταξίδι δημιουργικότητας και προσωπικής εξέλιξης που φτάνει μέχρι εδώ και που μας δίδαξε να αγαπάμε την ευθύνη.

Τέλος δεν μπορώ να μην αναφερθώ σε όλους τους ανθρώπους που συνέβαλαν και συμβάλουν στην ζωή μου με τον καλύτερο τρόπο. Την παρέα μου που είναι εκεί κάθε στιγμή και που θέλω να είναι εκεί για πάντα. Την συνάδερφο Ματίνα που λειτουργεί ως πρότυπο για εμένα καθώς επίσης τα μέλη της οικογένειάς μου Ιωάννα, Χρυσούλα και Κώστα που αν και είμαστε μακριά μας ενώνει η αγάπη, η αξιοπρέπεια και η προκοπή.

Νικόλαος Κορφιιάτης

## **Abstract**

HP-Nb modified steel is a cast heat resisting austenitic alloy, commonly used in reformer tubes working at temperatures 900-950 °C, because of the appealing combination of creep strength and oxidation resistance. However, material's microstructure degrades - due to high temperature service-leading to creep failure. The aim of this work was to reconstruct the 3D variations of the microstructure and correlate specific microstructural features to the creep behavior of the material.

The microstructure had been reconstructed in a software, which had used eight serial metallographies of a specimen. During the procedure there were difficulties that one has to deal with. Finally, a model of a total height 600µm created which contained information about the alloy's structure. It had been decided to enrich the experimental part with SEM and EDS analysis, as well as micro hardness tests at the carbides, for identification purposes.

In addition, some initial fundamental computational simulations had been employed to add important information that will help to form a complete approach of microstructure.

Data from citations, 3D model, EDS and microstructure and simulations were compared. Most of the results converge and only some of them present controversy. The conclusion of the work has revealed a complex multidimensional network of carbides, of specific volumetric fraction, hardness and composition. The combination of the data that had been acquired, created an even more integrate aspect of the microstructure and the behavior of the alloy.

## Περίληψη

Ο χάλυβας HP-Nb είναι ένα κράμα υψηλής αντοχής στην θερμοκρασία, του οποίου η χρήση συνηθίζεται σε αυλούς μονάδων αναμόρφωσης, σε θερμοκρασίες λειτουργίας που κυμαίνονται μεταξύ 900-950°C, λόγω του ότι συνδυάζει υψηλή αντίσταση σε ερπυσμό και σε οξειδωτικό περιβάλλον. Ωστόσο, λόγω της μακράς έκθεσης σε υψηλή θερμοκρασία η μικροδομή υποβαθμίζεται και οδηγείται σε αστοχία λόγω ερπυσμού. Σκοπός της παρούσας εργασίας είναι η τρισδιάστατη απεικόνιση της μικροδομής του χάλυβα αυτού και ο συνδυασμός της με δεδομένα της μικροδομής που αφορούν την συμπεριφορά του υλικού σε ερπυσμό.

Η μικροδομή μοντελοποιήθηκε σε λογισμικό, χρησιμοποιώντας οκτώ μεταλλογραφίες από ένα δοκίμιο στην σειρά. Στην διαδικασία αυτή υπήρξαν εμπόδια τα οποία πρέπει κανείς να ξεπεράσει ή και να συμβιβαστεί με αυτά. Εν τέλει, ένα τρισδιάστατο μοντέλο ύψους 600μm δημιουργήθηκε το οποίο περιέχει πολλά και ενδιαφέροντα δεδομένα για το κράμα. Η μελέτη εμπλουτίστηκε με μετρήσεις σκληρότητας και χημικές αναλύσεις για την ταυτοποίηση των καρβιδίων που εντοπίζονται στο κράμα.

Ακόμη, διεξήχθησαν κάποιες θεμελιώδεις και απλές υπολογιστικές προσομοιώσεις για να δημιουργηθεί μια καλύτερη προσέγγιση για την μικροδομή.

Όλα τα δεδομένα από δημοσιεύσεις, από το μοντέλο, τις μικροσκληρομετρήσεις, τις χημικές αναλύσεις και το υπολογιστικό κομμάτι, συγκρίθηκαν. Τα περισσότερα δεδομένα έδειξαν μεταξύ τους σύγκλιση αλλά δεν παρουσίασαν ταύτιση. Το συμπέρασμα είναι ένα πολυδιάστατο και σύνθετο δίκτυο καρβιδίων, τα οποία μελετήθηκαν και παρουσιάζουν συγκεκριμένο κλάσμα όγκου, σκληρότητα, σύσταση, συμμετοχή στο κράμα. Ο συνδυασμός όλων των δεδομένων που εξήχθησαν, δημιουργεί μια πιο ολοκληρωμένη άποψη για την μικροδομή και την συμπεριφορά του κράματος.



# Table of Contents

<b>CHAPTER 1</b>	<b>- INTRODUCTION .....</b>	<b>16</b>
1.1	AIM AND STRUCTURE OF DIPLOMA THESIS .....	16
1.2	CASE DESCRIPTION .....	16
1.3	CREEP RESISTANT ALLOYS.....	17
1.4	3D RECONSTRUCTION .....	18
1.5	SEM/EDS AND MICROHARDNESS MEASUREMENTS .....	18
1.6	COMPUTATIONAL THERMODYNAMIC CALCULATIONS.....	18
<b>CHAPTER 2</b>	<b>- LITERATURE REVIEW .....</b>	<b>20</b>
2.1	CREEP.....	20
2.2	3D DISPLAY .....	21
2.3	ALLOY H39WM.....	24
<b>CHAPTER 3</b>	<b>- EXPERIMENTAL.....</b>	<b>28</b>
3.1	3D RECONSTRUCTION.....	28
3.2	RESULTS .....	32
3.3	SEM/EDS ANALYSES .....	41
3.4	MICROHARDNESS MEASUREMENTS .....	44
<b>CHAPTER 4</b>	<b>- COMPUTATIONAL SIMULATION .....</b>	<b>46</b>
4.1	SCHEIL-GULLIVER SIMULATION .....	46
<b>CHAPTER 5</b>	<b>- DISCUSSION AND CONCLUSIONS.....</b>	<b>50</b>
5.1	DISCUSSION .....	50
5.2	CONCLUSION.....	51
<b>CHAPTER 6</b>	<b>- FUTURE WORK .....</b>	<b>52</b>
<b>CHAPTER 7</b>	<b>- BIBLIOGRAPHY .....</b>	<b>54</b>



## Tables

Table 2-1 Typical composition of HP-Nb modified alloy.....	24
Table 3-1 Microhardness values. ....	44
Table 4-1 Mn and Si are missing. When Scheil simulation attempted with the bulk chemical composition the output was not reasonable, so it had been decided to simplified, by keeping only the crucial elements.....	46



## Figures

Figure 1-1 [1] Furnace's tubes with crack.( Inside the cracks Ni-based catalyst is detected) .....	17
Figure 1-2 [2] View of creep resistant alloy's evolution over the years .....	17
Figure 2-1 [19] Creep classification curve.....	21
Figure 2-2 Specimen from the tube .....	21
Figure 2-3 [4] 3D reconstruction of melanoma cell nuclei .....	22
Figure 2-4 a) Focused Ion Beam deducts layer for 3D EBSD technique. b) X-ray micro tomography process .....	22
Figure 2-5 [5] The black arrow indicates an austenite grain .....	23
Figure 2-6 [6] (a) Gas pore (b) Shrinkage pore in section view .....	23
Figure 2-7 [7] As-cast condition of HP modified alloy .....	24
Figure 2-8 [7] EBSD map of M7C3 to M23C6 transformation .....	25
Figure 2-9 [9] SEM image of G-phase close to MC .....	25
Figure 3-1 At the bottom the OD is shown. The characteristic sign at bottom left with the crack in the middle are the signs to track the frame. ....	29
Figure 3-2 (a) Inside the carbide network there is an austenitic grain. A trace is drawn by clicking along the boundary (b) the process is repeated for all the layers (c) the software creates a volume by lofting the traces .....	29
Figure 3-3 Flow chart of the preparation process .....	30
Figure 3-4 Layer distance diagram.....	30
Figure 3-5 The metallographies show the evolution of the microstructure in space. a) the first section h) last section .....	31
Figure 3-6 Side view of the 3D microstructure. ....	32
Figure 3-7 Front view of the 3D model, which corresponds to the frame shown in Fig 3.5a. ....	32
Figure 3-8 Rear view of the 3D model, which corresponds to the frame shown in Fig 3.5h .....	33
Figure 3-9 3D view of the primary carbides network. The green and read areas correspond to austenite matrix. ....	33
Figure 3-10 White arrows indicate creep cracks (tertiary creep) while black arrows point to the remaining primary carbides.....	34

Figure 3-11 Arrow indicates an inter-dendritic carbide that penetrates inside the matrix .....	34
Figure 3-12 The carbide network.....	35
Figure 3-13 3D model of cracks .....	35
Figure 3-14 3D model of cracks combined with carbide network.....	36
Figure 3-15 A common way to reproduce quickly and easily a 3D view and in this case is used to compare results with the software output. It is quite impressive the evolvement of the crack. 37	
Figure 3-16 Comparison of 3D model with metallography (side view).....	37
Figure 3-17 (a) Rod like eutectic M7C3 carbides (b) 3D model reconstruction of M7C3 carbides .....	38
Figure 3-18 Volumetric measurements .....	38
Figure 3-19 The volume fraction calculation from software. 95% Austenite and 5% Carbides... 38	
Figure 3-20 Microhardness measurement at carbide that was illustrated in 3D model. 1530 HV <sub>0.01</sub> .....	39
Figure 3-21 Microhardness measurement at carbides that were illustrated in 3D model. a) 1600 HV <sub>0.01</sub> b) 1080 HV <sub>0.01</sub> .....	40
Figure 3-22 a) Optical microscope capture of the carbide b) The X-ray map of the same carbide indicates that white region at the left of the carbide is Nb carbide and the carbide in the middle of the image is Cr-rich carbide.....	41
Figure 3-23 Spectrum 3, denotes M23C6 carbide. Spectrum 1 and 2 denote MC carbide.....	42
Figure 3-24 Spectrum 1, 2 and 3 indicate composition M7C3. ....	42
Figure 3-25 Spectrum 1 corresponds to M23C6 and Spectrum 3 to M7C3. This result confirms the literature reports about M7C3 transformation. ....	42
Figure 3-26 Spectrum 1,2,3 and 6 indicates M7C3 stoichiometry .....	43
Figure 3-27 Spectrum 1,2,3 correspond to M7C3 composition .....	43
Figure 3-28 The guide shows the number and the position of each measurement .....	44
Figure 3-29 The relative values suggest that Cr7C3 has higher hardness than Cr23C6. ....	45
Figure 3-30 The black arrows indicate measurements at characterized carbides as M7C3. Blue arrow indicates a measurement which corresponds at M23C6 carbide.....	45

Figure 4-1 The Scheil-Gulliver diagram with “Global Minimization” indicates solidification sequence Austenite, M7C3, MC, M23C6. The dotted line is the equilibrium line which is the solidification according to phase diagram .....	47
Figure 4-2 The Scheil-Gulliver diagram without “Global Minimization” indicates solidification sequence Austenite, M7C3, M23C6, MC. ....	48



## Chapter 1 - Introduction

### 1.1 Aim and structure of Diploma Thesis

The aim of this work is to present a complete study of a 3D metallography of the creep resistant alloy H39WM which had failed prematurely during service due to accidental overheating. The alloy was installed in a Hydrogen reformer unit and the total service life before the accident was 5 years. The 3D reconstruction of the alloy microstructure and the representation of the creep damage in 3D is going to provide a more integrated aspect of the alloy behavior under creep damage.

The current thesis consists of 5 chapters:

In the **1<sup>st</sup> chapter**, the reader is being introduced to the contents of the thesis and a brief presentation of the installation where the incident took place is given.

In the **2<sup>nd</sup> chapter**, a literature review on creep phenomena, 3D construction methods, as well as H39WM properties and microstructure is presented.

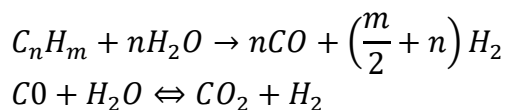
In the **3<sup>rd</sup> chapter**, the 3D model is presented and thorough details on the construction method followed are provided. In addition, characterization work including metallography microhardness measurements and SEM/EDS analyses are also presented.

In the **4<sup>th</sup> chapter**, some preliminary results concerning a Computational Thermodynamic analysis are shown.

In the **5<sup>th</sup> chapter**, the work is concluded and discussion on the relevant results is given. In addition, some recommendations for future work are highlighted.

### 1.2 Case description

**Steam reforming** or **steam methane reforming** is a chemical synthesis for producing syngas (hydrogen and carbon monoxide) from hydrocarbons such as natural gas. This is achieved in a reformer which reacts steam at high temperature and pressure with methane in the presence of a nickel catalyst. The steam methane reformer is widely used in refineries to produce hydrogen. (Figure 1.1). The relevant chemical reactions are shown below:



Centrifugally cast tube dimensions: ID 103.3mm, OD 136mm, Thickness 15.45mm

Normal Operating Conditions: Temperature: 910 °C, Pressure: 30 bar

A malfunction at part of furnace's equipment caused accidental overheating in a very short time that led in creep failure. Figure 1.1 [1] shows an example of reformer tubes that had failed.

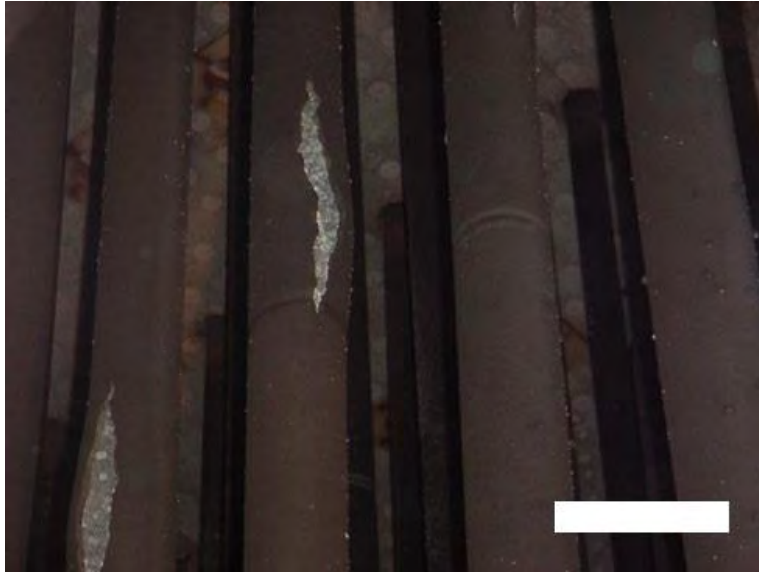


Figure 1-1 [1] Furnace's tubes with crack. (Inside the cracks Ni-based catalyst is detected)

### 1.3 Creep resistant alloys

From the beginning of the previous century, power plants had demanded higher resistance at high temperatures for the materials, in order to achieve higher efficiency. In combination with corrosion resistance demands, micro alloyed steels had been developed, in order to operate at critical temperatures and environments (vapor production, furnaces). Elements such as Chromium and Nickel -commonly used at heat and corrosion resistant steels- Niobium and Titanium are responsible for these properties.

Based on Fe-35Ni-25Cr steel, many micro alloys had been developed, by adding the elements that had been referred. Figure 1.2 [2] shows creep resistant alloy's evolution.

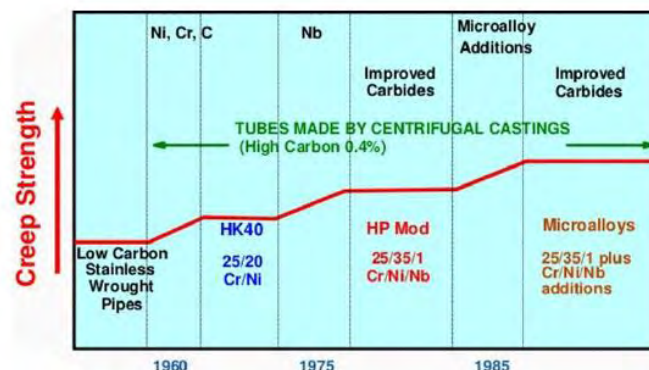


Figure 1-2 [2] View of creep resistant alloy's evolution over the years

## **1.4 3D reconstruction**

The 3D representation of metallic materials microstructure provides a complete view over the classical 2D approach. In the current case the evolution of the creep damage (microcracks, voids) along with the associated microstructural features of the cast alloy were experimentally investigated to reveal their spatial distribution. In the literature some methods are reported for creating the 3D model, either destructive e.g. sequential sectioning metallography or non-destructive as X-ray computed tomography. In our knowledge this is the first time that a 3D model based on sequential sectioning has been attempted for revealing the creep failure in tubes that were used in high temperature service. In this context, the approach adopted within the current thesis is based on the composition of a certain series of 2D metallographies to create the 3D model of the microstructure.

## **1.5 SEM/EDS and Microhardness Measurements**

In addition to 3D metallography the microstructure was further characterized by employing SEM/EDX analyses and microhardness measurements in order to assess local composition and micromechanical properties of the phases composing the microstructure.

## **1.6 Computational Thermodynamic Calculations**

ThermoCalc was employed for conducting preliminary calculations on the phases existing in the microstructure.



## Chapter 2 - Literature Review

### 2.1 Creep

Creep is a time dependent deformation under a certain applied load which occurs at elevated temperature. As a result, the material undergoes a time dependent increase in length, which could be dangerous in service. The phenomenon is usually encountered in parts such as turbomachinery fans (designed to be lightweight as they are rotating parts), tubes of fired heaters and generally heat exchanger tubes.

Plastic deformation, besides the atomic bond relaxation, is also caused by the dislocation motion. At high temperatures, dislocations can move more easily, as diffusion phenomena are taking place. In fact, creep is strongly connected with diffusion mechanisms, thus it explains the time dependence of creep deformation.

Two types of creep have been established, the dislocation creep and the diffusional flow. Dislocation creep can be described as the dislocation motion assisted from the climbing phenomenon, which has been thermally activated. On the other hand, diffusional flow is related to cases of low stresses (and high temperatures) and so it has no contribution from dislocation movements. Deformation is only affected by diffusional phenomena of cavities and atoms. The mathematical relations (rate of deformation to stress) of these two types of creep confirm these observations [3]:

Dislocation creep:  $\frac{d\varepsilon}{dt} \sim D * \sigma^m$

Diffusional flow:  $\frac{d\varepsilon}{dt} \sim D * \sigma$

Specific design parameters are capable of affecting the creep resistant behavior of alloy. These parameters could be: crystal structure, melting point, grain size, as well as alloying additions. A common example is a turbine blade, that operates at extremely high temperatures and it is loaded due to rotational motion. Nowadays, blades are made from special Nickel alloys containing the  $\gamma$ -phase ( $\text{Ni}_3\text{Al}$ ) which provides resistance at dislocation motion and is very stable even at high temperatures.

The creep evolution typically shows three stages: primary, secondary and tertiary (Fig. 2.1)

- Primary Creep: starts at a rapid rate and slows with time.
- Secondary Creep: has a relatively uniform rate.
- Tertiary Creep: has an accelerated creep rate and terminates when the material breaks or ruptures.

Typical tertiary creep damage is presented in specimen of Figure 2.2, which is the specimen that was used in this work.

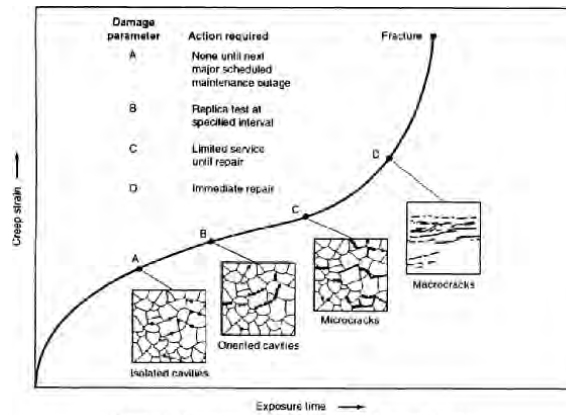


Figure 2-1 [19] Creep classification curve

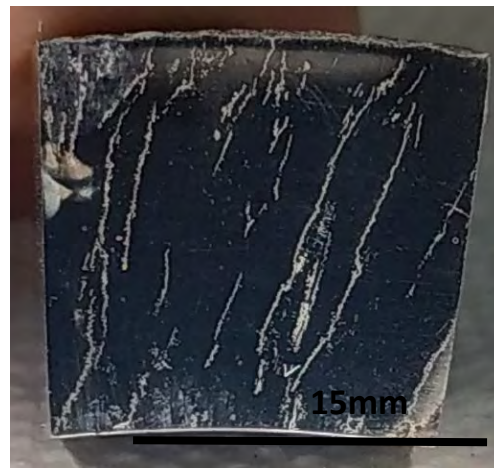


Figure 2-2 Specimen from the tube

## 2.2 3D Display

Metallography allows researchers to investigate the microstructure of a material. The most widely used is 2D metallography which can quantify details of the microstructure. Intermetallic compounds, phases and precipitates are some common features that can be observed with the 2D metallography. However, it is essential to represent the spatial distribution of the several features, in other words to develop 3D representation of the microstructure. Nowadays, many sciences such as neurology, archeology and biology use 3D models to display their findings. Metallurgy uses 3D models to extract information about grain's size and shape, grain growth or volume fraction estimation.

The first method that had been implemented is a manual process called "serial sectioning method". Its philosophy is to compose many 2D metallography sections. It is time consuming process, as it demands many steps to accomplish the final model. However, the major disadvantage is the low functionality in detailed view. So, if the microstructure consists of complicated phases, for example martensite or fine precipitates, serial sectioning method

does not provide high quality model. In this thesis, this is the method that was followed as all the tools to create the 3D model with this technique were available. Also, it should be noted that images from optical microscope, SEM or TEM can be used for the reconstruction. Figure 2.3 [4] presents the result of 3D reconstruction of melanoma cell nuclei from a series of 50 consecutive sections of 100nm. That specific project used the same 3D construction software to the one that had been used at the present work.

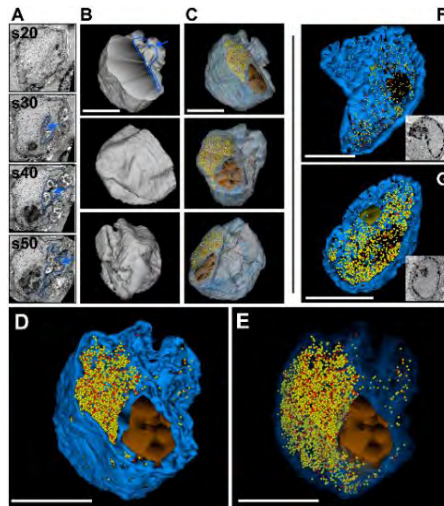


Figure 2-3 [4] 3D reconstruction of melanoma cell nuclei

The other 3D reconstruction techniques are more advanced, sophisticated and automatic. For example, 3D EBSD which is sometimes also referred to as EBSD tomography is a 3D-orientation microscopy method that works by sequential serial sectioning in a FIB-SEM, by serial polishing or sequential layer ablation by Laser Electron Back-Scattered Diffraction (EBSD). As shown in Figure 2.4, ion beam is used to mill away the surface between each EBSD map. That method approaches a maximum 3D reconstructed volume of  $50 \times 50 \times 50 \mu\text{m}^3$  and the quality of the result of this method in very low magnification is remarkable. Figure 2.5 [5] shows 3D EBSD application at microstructure of medium-Mn steel created from 95 slices.

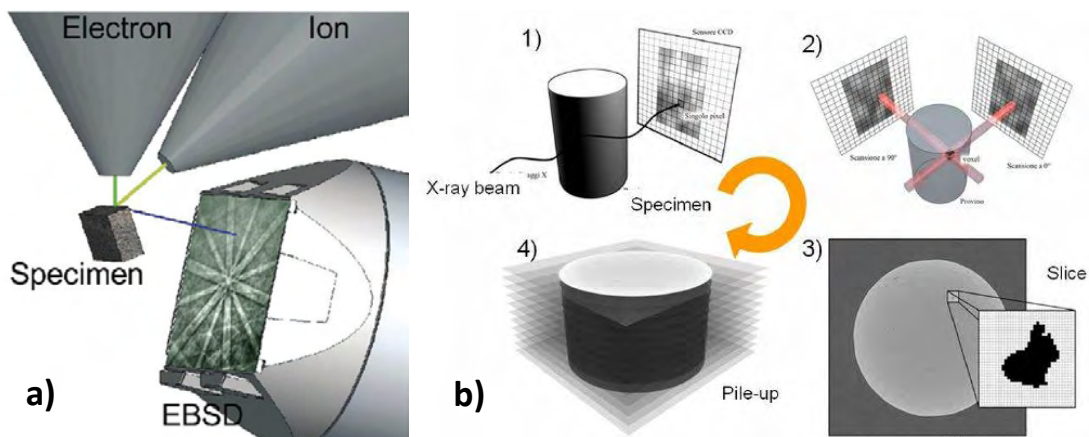


Figure 2-4 a) Focused Ion Beam deduces layer for 3D EBSD technique. b) X-ray micro tomography process

In addition, there is one more well-known method, the X-ray computed tomography (XCT). A difference with the previous methods is that XCT is considered as a non-destructive method. XCT exploits the penetrating ability of high density focused X-ray beam, which is applied at a rotating sample. An electronic high resolution detector system is used for image acquisition as shown in Figure 2.4. In Figure 2.6 [6], the 3D reconstruction of two kind of pores in cast Al-Si alloy, are presented with XCT method. This reconstruction had been used to conduct Finite Element Analysis on a specimen that includes these pores.

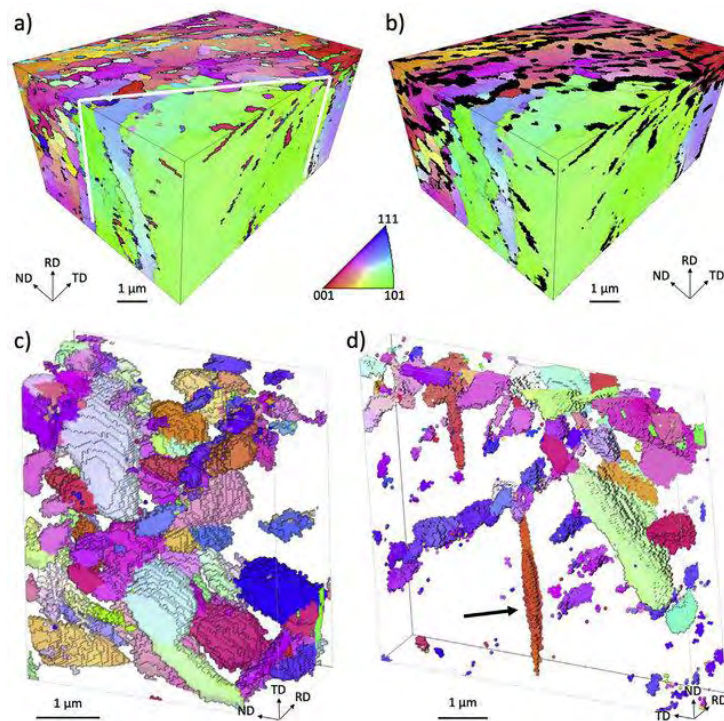


Figure 2-5 [5] The black arrow indicates an austenite grain

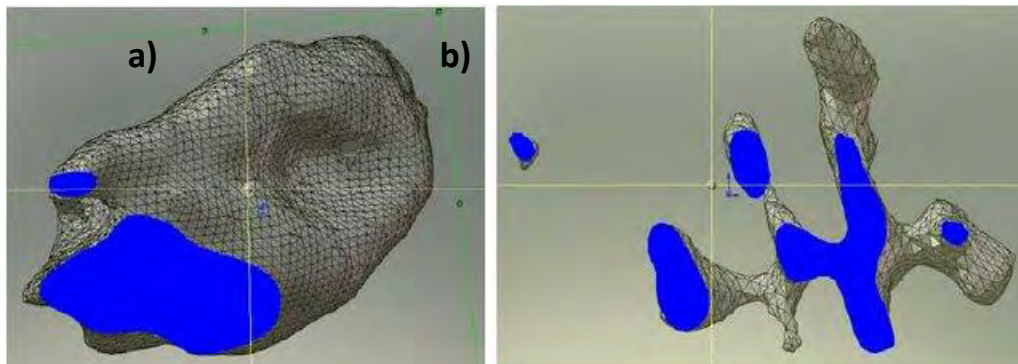


Figure 2-6 [6] (a) Gas pore (b) Shrinkage pore in section view

### 2.3 Alloy H39WM

H39WM is a high creep and temperature resistant alloy and is based on Fe-25Cr-35Ni steel. Its predecessor was the HP-40 alloy. The composition is presented at Table 2.1. Since Ni ( $\gamma$ -stabilizer) content is high, open austenitic region is created in the phase diagram. Centrifugal casting, results in austenitic dendritic grains oriented in the radial direction from the inside diameter towards the outside diameter of the tube. The material is strengthened by a network of primary interdendritic carbides. Cr improves corrosion resistance by forming a thin film of Cr rich oxide on the surface, but the significant effect of Cr-addition is the formation of Cr-rich carbides that improve mechanical properties. Nb is added for the precipitation of NbC, which due to its thermal stability contributes to increased creep resistance and in addition to prevent  $\delta$  phase precipitation.

Table 2-1 Typical composition of HP-Nb modified alloy

C	Si	Mn	P	S	Cr	Ni	Nb	Mo	Ti	Fe
0.38-0.45	0.5-1.5	0.5-1.5	0.02	0.01	24-27	34-37	0.7-1.3	0.07	0.05-0.3	Balance

The composition of Table 2.1 results in, as-cast condition, at a microstructure consisted from the austenitic matrix and primary carbides as shown in Figure 2.7. These carbides are Cr-rich and Nb-rich. According to the literature [7] Cr-rich primary carbides have stoichiometric composition  $M_7C_3$  (but there are references that mention  $M_{23}C_6$  too) and Nb carbides have MC stoichiometry.

After extended service exposure above 800 °C degradation, aging and phase transformation can occur [8]. In fact, the  $M_7C_3$  to  $M_{23}C_6$  transformation (Figure 2.8) and the  $M_{23}C_6$  and MC coarsening are the phenomena that affect the material properties. During elevated temperature service decomposition of  $M_7C_3$  promotes  $M_{23}C_6$  precipitation [7]. It has been also observed that NbC at aged condition are larger in size at the as-cast condition due to coarsening.

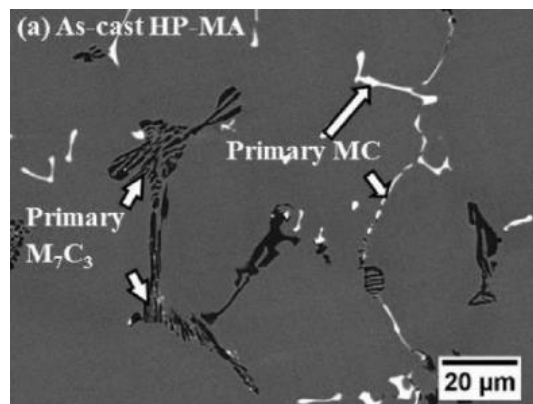


Figure 2-7 [7] As-cast condition of HP modified alloy

Another notable phenomenon is G-phase transformation (Figure 2.9) [9] from MC carbides. It is not presented in the studied case but it is worth mentioned. As G-phase transformation occurs from outside and continues towards the center of MC carbide and G-phase cannot dissolve Ti, this element seems to control the process [10]. At that point, it is important to mention that the interface between G-phase and matrix is preferential site for occurrence of creep damage. Its stoichiometry is  $\text{Ni}_{16}\text{Nb}_6\text{Si}_7$ .

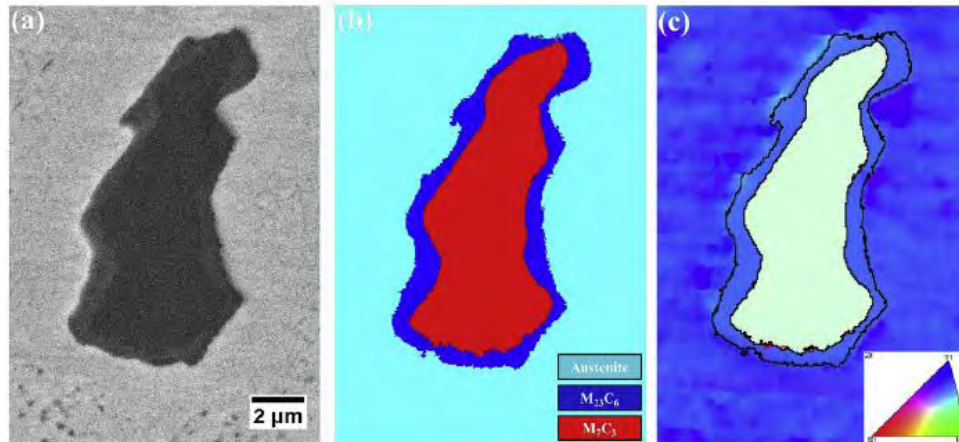


Figure 2-8 [7] EBSD map of  $\text{M}_7\text{C}_3$  to  $\text{M}_{23}\text{C}_6$  transformation

Cr- rich carbides are mainly the  $\text{M}_7\text{C}_3$  (in the as-cast condition) or  $\text{M}_{23}\text{C}_6$ . Both are lying in a dendritic pattern that forms a carbide network along grain boundaries. Their shape and size varies. For example,  $\text{M}_7\text{C}_3$  seems to have eutectic and lameloid appearance. On the other hand,  $\text{M}_{23}\text{C}_6$  has probably a chain like form.

Carbon content is higher in  $\text{M}_7\text{C}_3$  than  $\text{M}_{23}\text{C}_6$  that has more Fe and Ni. Also,  $\text{M}_{23}\text{C}_6$  that has been characterized as more thermodynamically stable than  $\text{M}_7\text{C}_3$ , nucleates intergranularly and intragranularly on defects as dislocations and twins. Moreover, it had been find out that its structure is FCC and it has coherency with the matrix, which is important for the alloy's behavior at elevated temperature. As for the  $\text{M}_7\text{C}_3$ , it has an orthorhombic crystal structure that does not reveal coherency with the matrix.

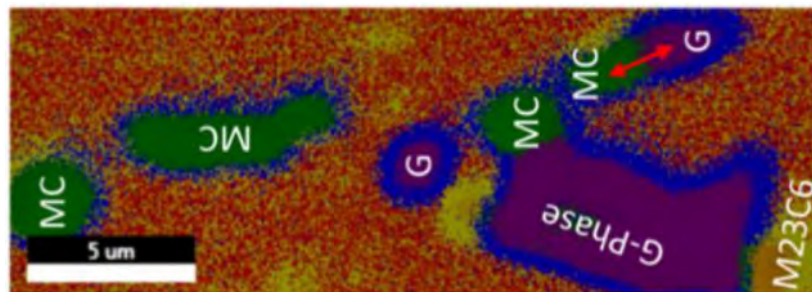


Figure 2-9 [9] SEM image of G-phase close to MC

Nb carbides have an important role. They are located within the matrix but also at the grain boundaries in a sparse distribution. Their crystal structure is cubic. Although MC formation decreases the carbon content in matrix, there is enough remaining carbon for the secondary precipitation.

To conclude, this literature review leads to the following notes:

- Network carbide formation
- Intra-granular carbides are these that inhibit dislocation motion and Inter-granular carbides prevent grain boundary sliding
- The interface between carbides and matrix might be beneficial for crack growth. More specifically, MC and  $M_{23}C_6$  coherent but  $M_7C_3$  not coherent.
- Cr carbides are definitely more than NbC due to the higher Cr concentration as shown in Figure 2.10 [13]
- As cast material composes of austenite matrix,  $M_7C_3$  (mainly) and MC
- Important phenomena: G-phase,  $M_7C_3$  to  $M_{23}C_6$  transformation, coarsening

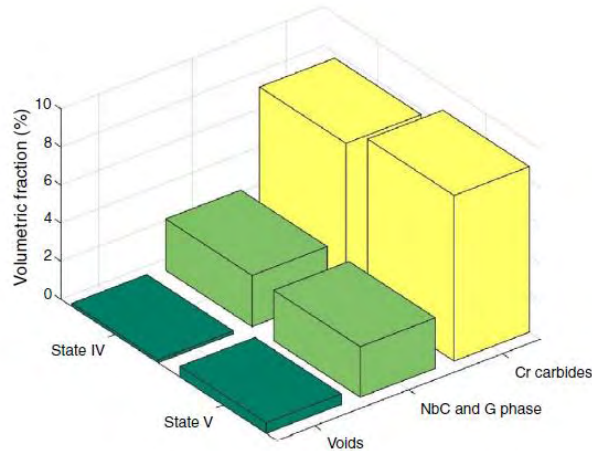
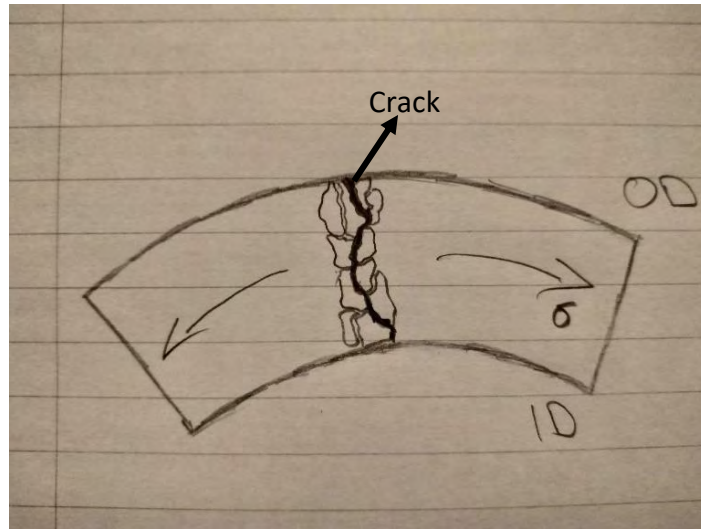


Figure 2-10 [13] Volumetric fraction of NbC, Cr carbides and voids

Last but not least, it should be mentioned that the centrifugal casting results in austenitic dendritic grains oriented in the radial direction from the ID towards OD. Also, creep cracking initiated at ID and propagated by linking cavities along the interdendritic carbide network, separating the dendritic grains (Figure 2.11). Therefore, the orientation of the grains that are perpendicular at hoop stresses seems to degrade creep resistance, from the moment of crack beginning. However, oriented grains with same direction with hoop stresses is not beneficial for creep resistance either.



*Figure 2-11 Hoop stress perpendicular with radial oriented grains, beneficial for crack*

## Chapter 3 - Experimental

### 3.1 3D Reconstruction

The aim of the present work, was the 3D reconstruction of the microstructure of a high creep resistant steel. The technique that had been followed is serial sectioning by careful metallographic grinding and polishing. It had been decided to create a model with thickness  $\sim 750\mu\text{m}$ . The software used to export a 3D model was the “Reconstruct” software, freely available at [14] <http://synapses.bu.edu/tools/>. This tool has been developed from the Department of Biology in Boston University, for research purposes.

Eight consecutive metallographies combined to create the model, but at least 30 metallographies conducted in order to accomplish the best quality at the images that are going to be used for the modeling.

As this is the very first time that a 3D reconstruction attempted by LoM, it should definitely leave a feedback for future exploitation of this method. For that reason, it is considered necessary to remark the major problems that obstruct or delay the process. These are mentioned and described below:

- i. Alignment of captured images
- ii. Compromise between magnification and resolution
- iii. Trace creation for every element that will be demonstrated

The process of the 3D model creation is about composing many 2D images. It is obvious that these images should illustrate exactly the same frame of the specimen. There are a few ways to accomplish that, for example by a microhardness trace that would be used as tracking sign. Another way is to take advantage of the geometrical and particular characteristics of the specimen, which is what it had been done in that case. More specifically, it had been decided to display a region right above the Outer Diameter in order to be located easily as shown in Figure 3.1.

Another issue that came up was the tradeoff between high resolution but small area of the picture and medium resolution but more wide depicted area. Firstly, the acceptable magnification was x100 (actually x100x0.8) that had the necessary resolution. However, this magnification limited the dimensions of the frame. As a result, carbides and austenitic grains of the image were not enough for the 3D model. Furthermore, x50 magnification had poor resolution, for the purpose of this work. So, the solution was to merge two x100 images of two consecutive frames. This step would add more time in the total process but it was necessary for the final result.

The last, time consuming step, was the tracing process in the software of every part of the metallography that it should be displayed. For example, if there is a carbide which is presented in all eight sections, then eight traces have to be created in order for the software to output a 3D object. Therefore, the final 3D assembly, which consists of 14 objects needs  $14 \times 8 = 112$  traces. Every trace is a closed contour which includes the element that will be presented. Figure 3.2 shows the trace of an austenitic grain in one layer and in all eight layers.

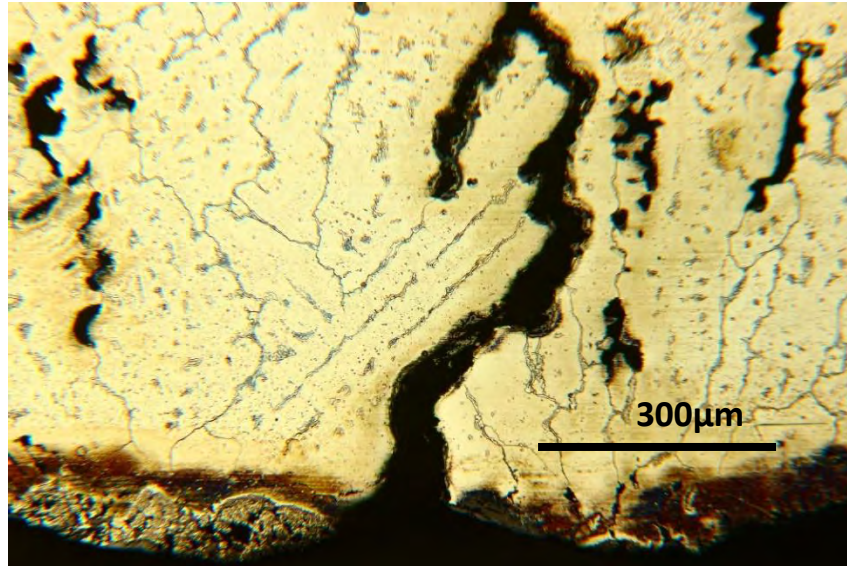


Figure 3-1 At the bottom the OD is shown. The characteristic sign at bottom left with the crack in the middle are the signs to track the frame.

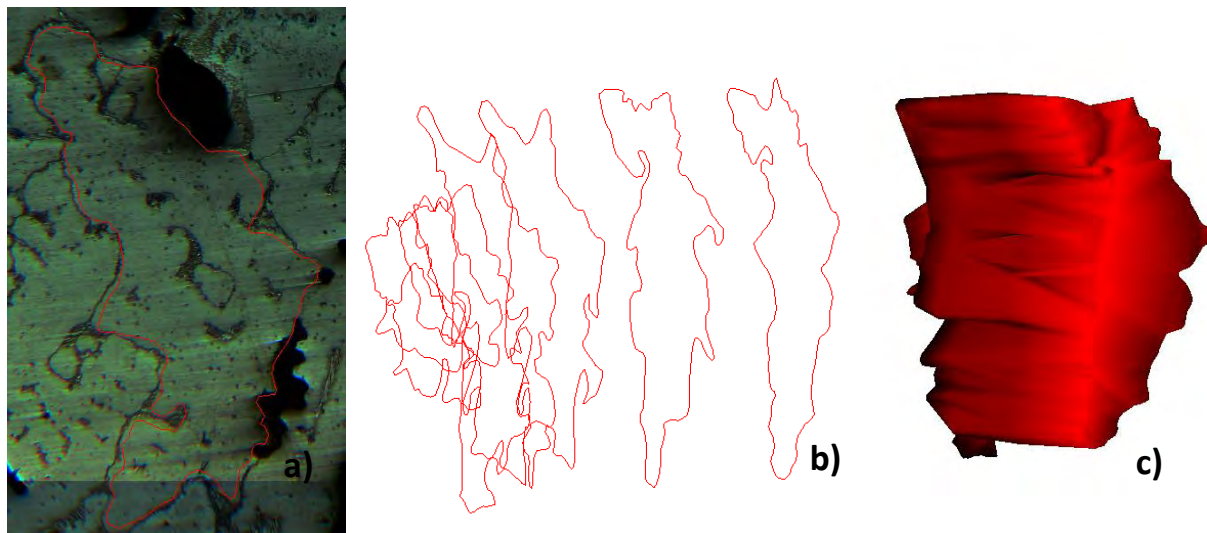


Figure 3-2 (a) Inside the carbide network there is an austenitic grain. A trace is drawn by clicking along the boundary (b) the process is repeated for all the layers (c) the software creates a volume by lofting the traces

At this point, it becomes clear that this process consumed a considerable amount of time. However, it is inevitable part of the process, unless there is a software smarter and quicker in this step, which could read and define the closed contours of the image on its own. To conclude, the final flow chart of the experimental work is shown below:



Figure 3-3 Flow chart of the preparation process

The total thickness investigated was  $600\mu\text{m}$ , approached by 8 sections between  $40\text{-}120\mu\text{m}$ . After each metallography a measurement by micrometer was conducted to evaluate the reduced thickness, with precision of  $3\mu\text{m}$ . The measurements indicated the distance between the layers are presented below:

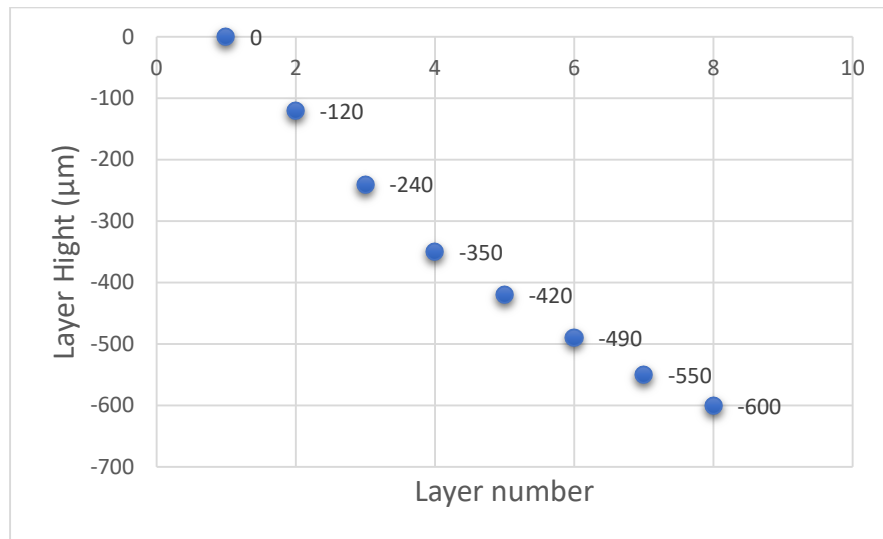


Figure 3-4 Layer distance diagram

As shown at the diagram the real thickness of the model was  $21990\mu\text{m} - 21390\mu\text{m} = 600\mu\text{m}$ .

At this point, it should be noted that the material removal was achieved via grinding with SiC papers of 800, 1000 and 2000 grit followed by polishing with  $1\mu\text{m}$  diamond paste. Microstructure revealed with Marbles reagent.

In the Figure 3.5, the eight metallographies that were inserted in the software are depicted, consisted from sixteen (16) images, merged two by two.

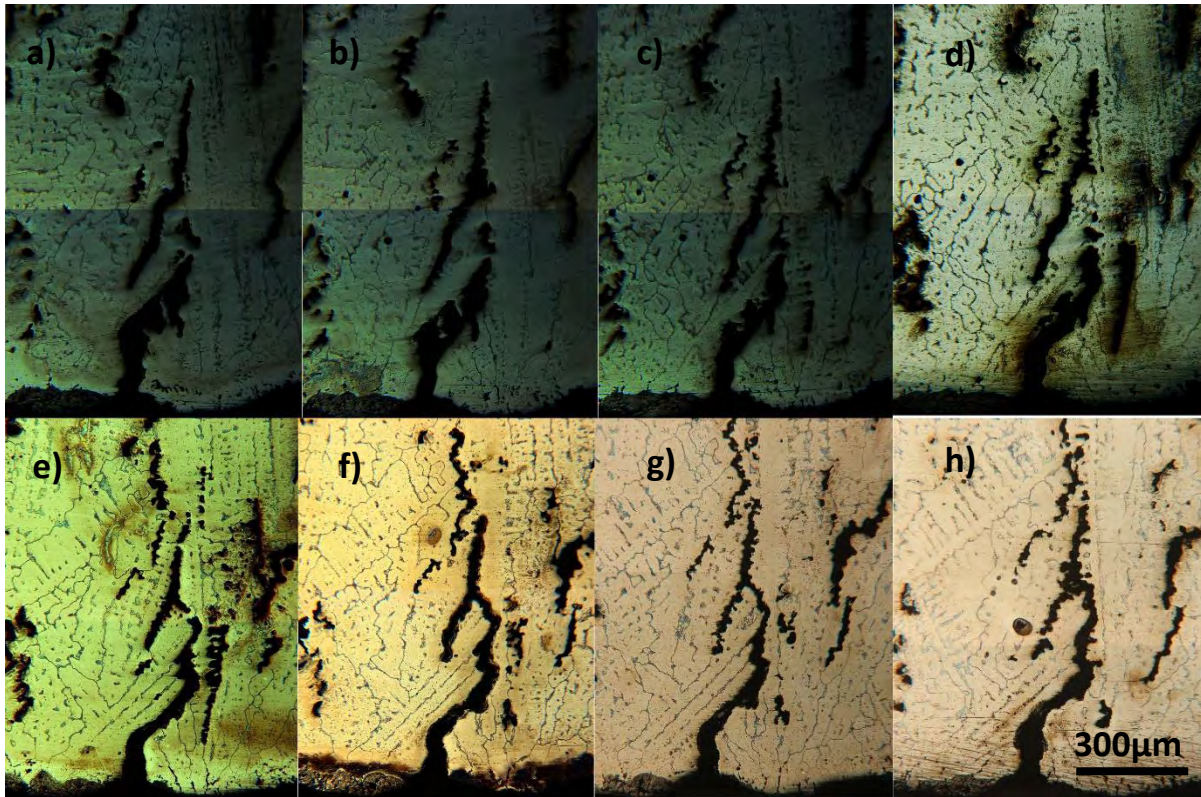
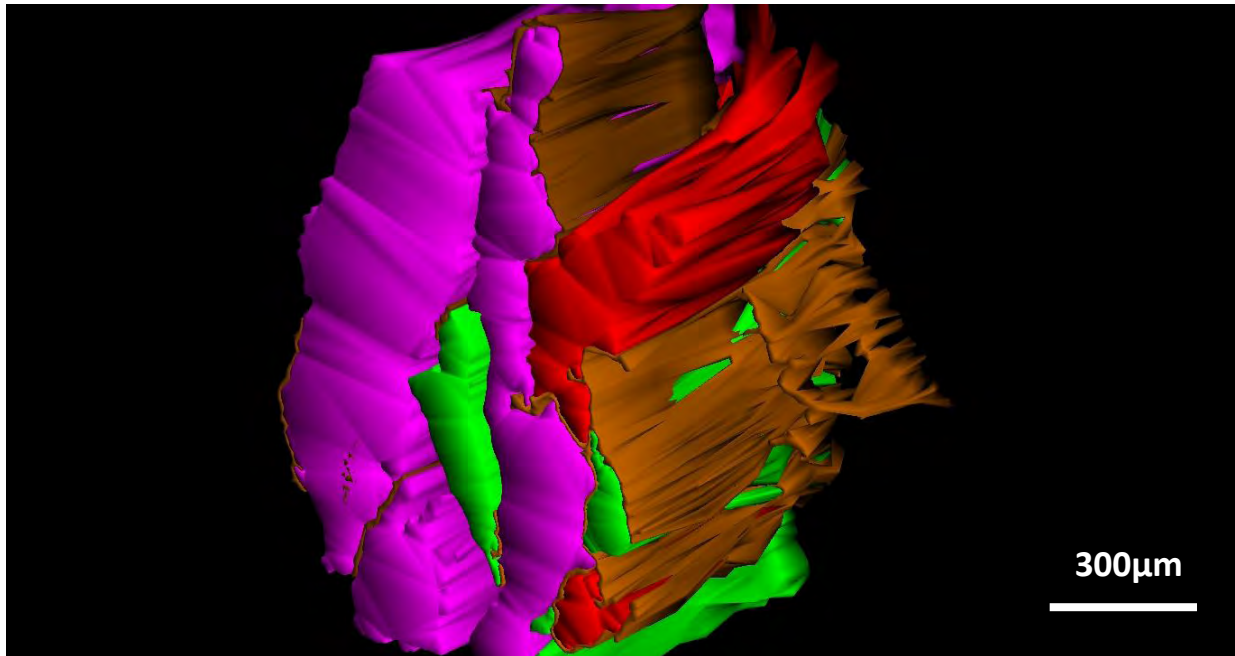


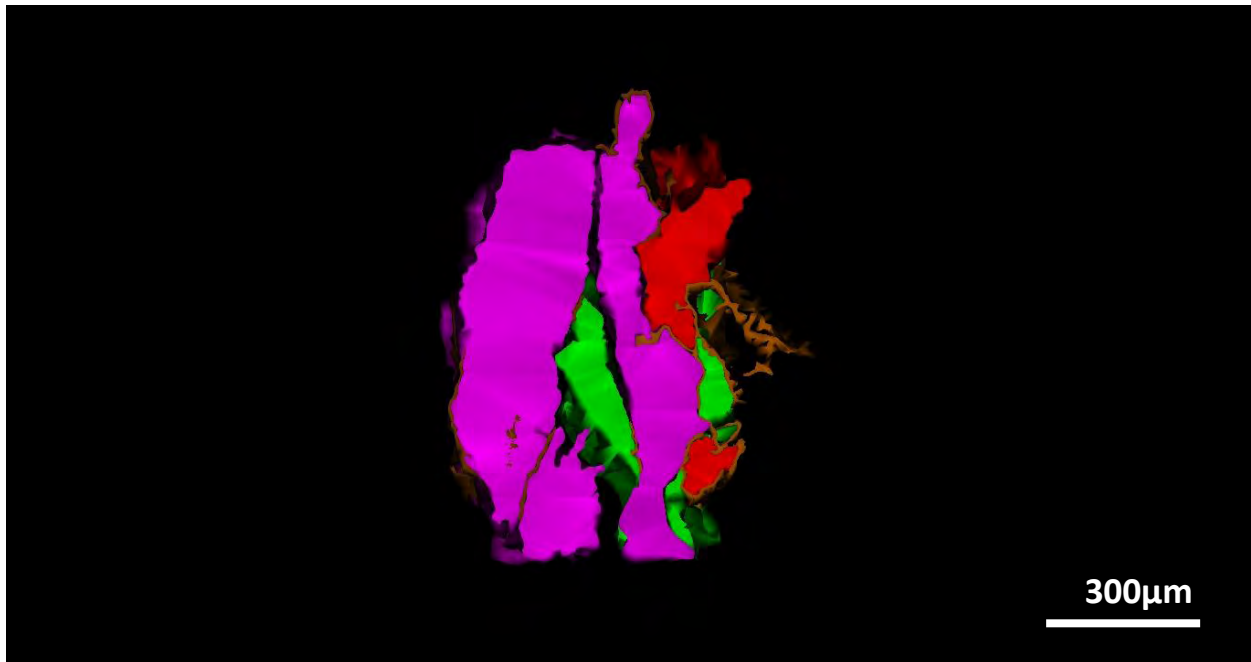
Figure 3-5 The metallographies show the evolution of the microstructure in space. a) the first section h) last section

## 3.2 Results

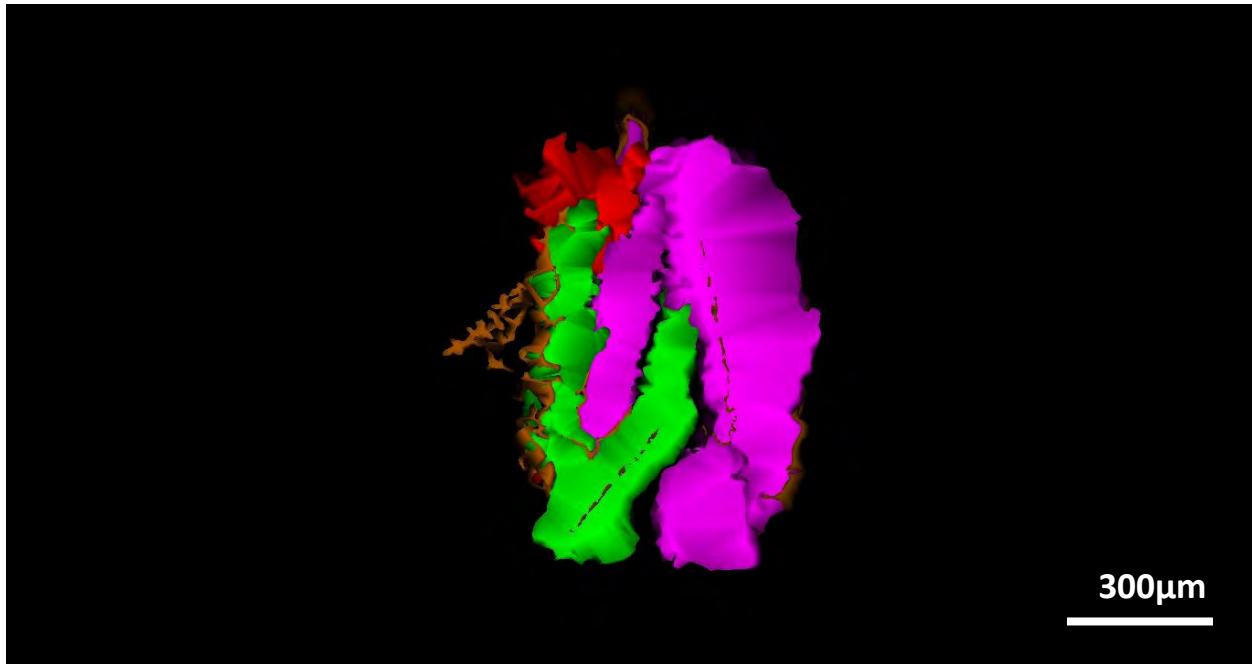
The 3D reconstructed model was developed and its characteristic results are displayed in Figures 3.6- 3.12 below. In Figure 3.13 and Figure 3.14 the cracks are presented in 3D perspective along with the carbides from the microstructure.



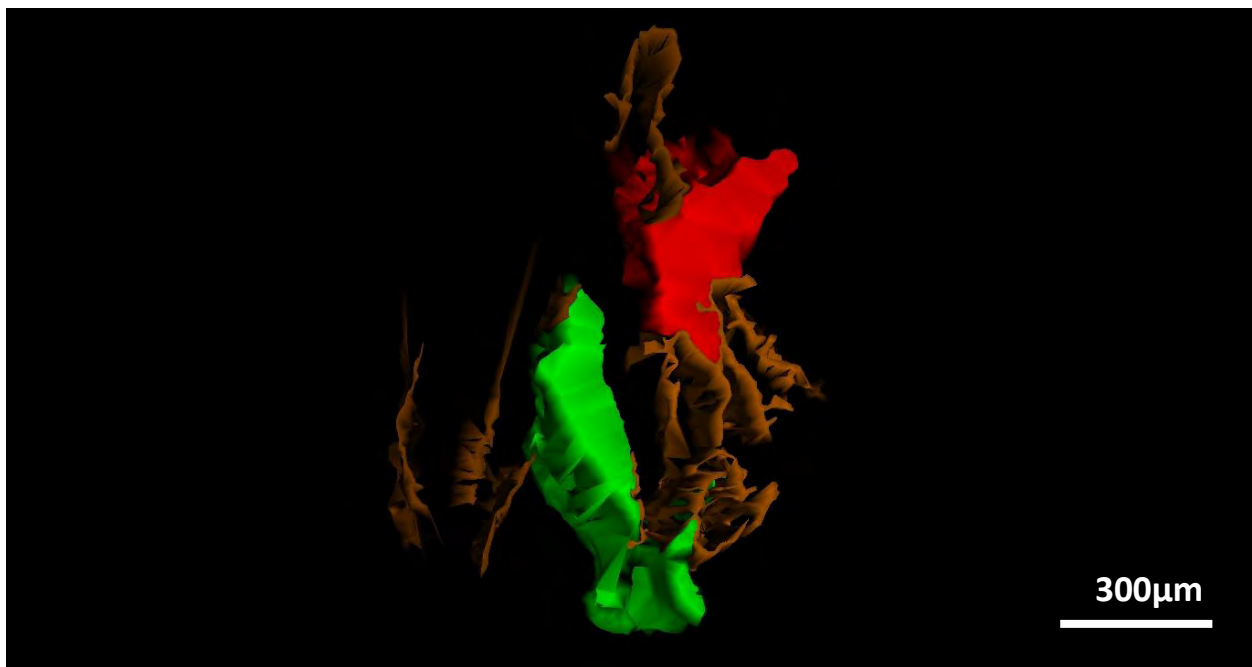
*Figure 3-6 Side view of the 3D microstructure.*



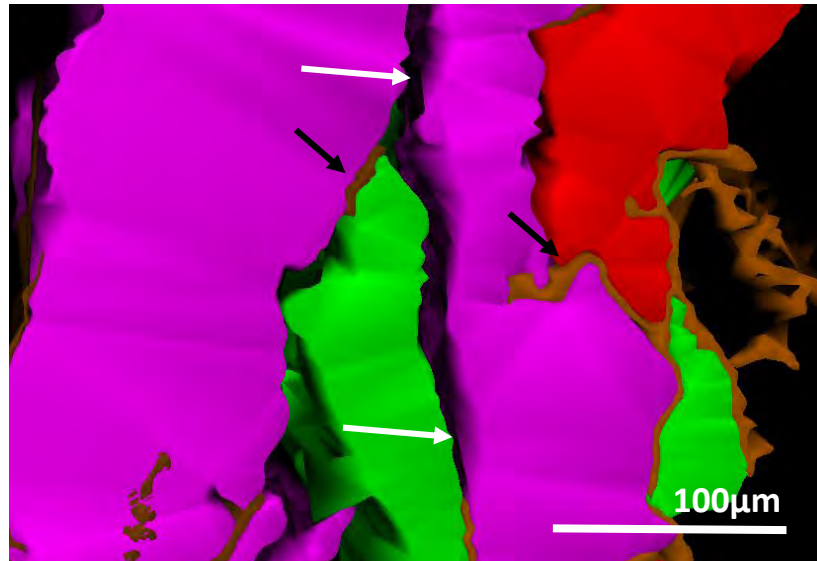
*Figure 3-7 Front view of the 3D model, which corresponds to the frame shown in Fig 3.5a.*



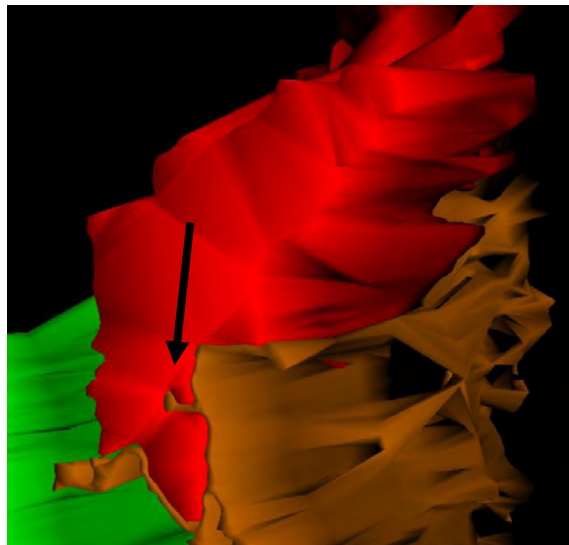
*Figure 3-8 Rear view of the 3D model, which corresponds to the frame shown in Fig 3.5h*



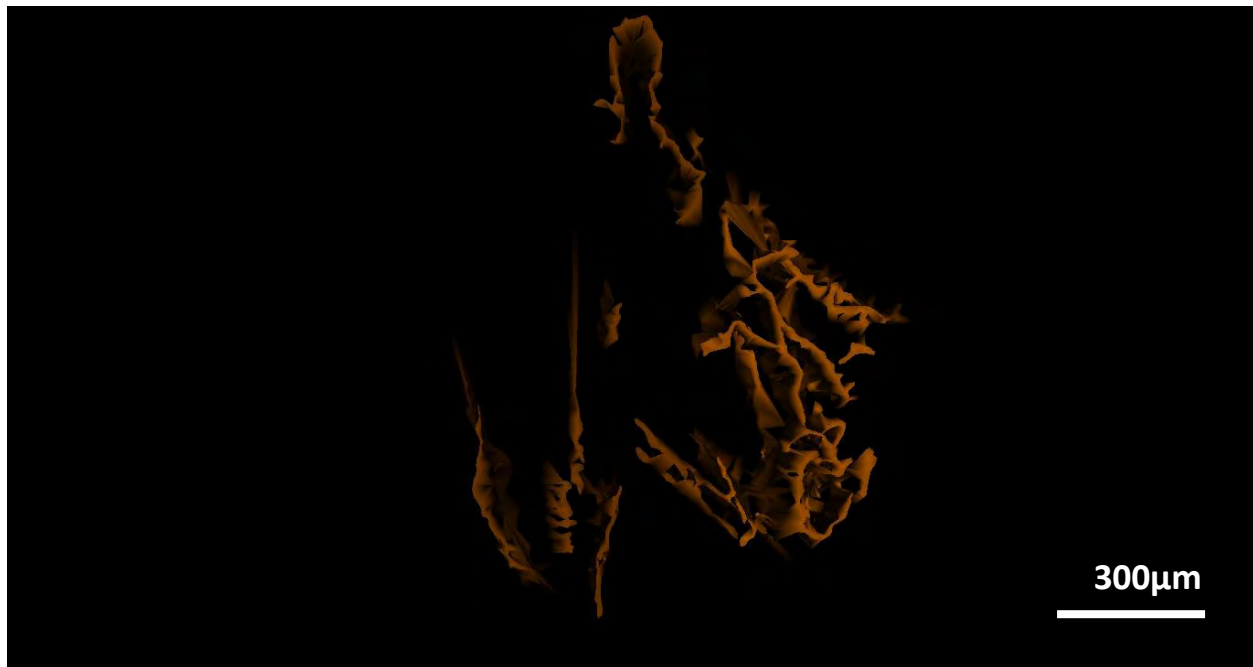
*Figure 3-9 3D view of the primary carbides network. The green and red areas correspond to austenite matrix.*



*Figure 3-10 White arrows indicate creep cracks (tertiary creep) while black arrows point to the remaining primary carbides*

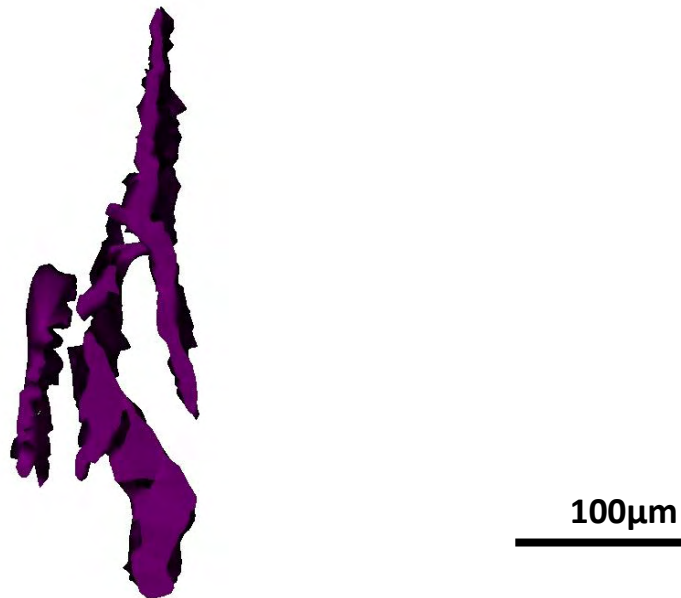


*Figure 3-11 Arrow indicates an inter-dendritic carbide that penetrates inside the matrix*

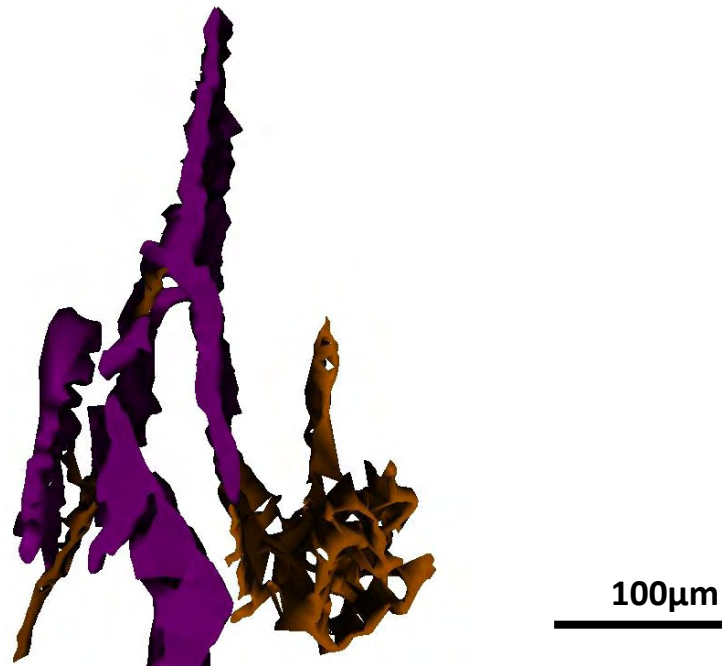


*Figure 3-12 The carbide network.*

Pervious Figures reveal that the primary carbide network operates as a supporting spaceframe to the austenite matrix. The network is multidirectional with significant thickness compared to the thickness of matrix. This is because the carbides are interconnected in space.



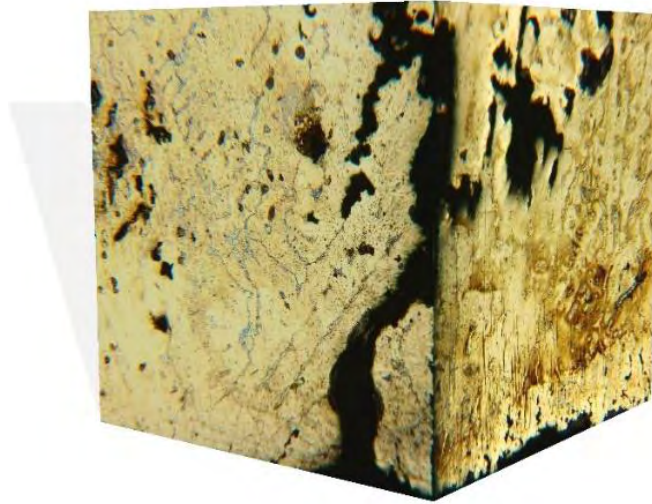
*Figure 3-13 3D model of cracks*



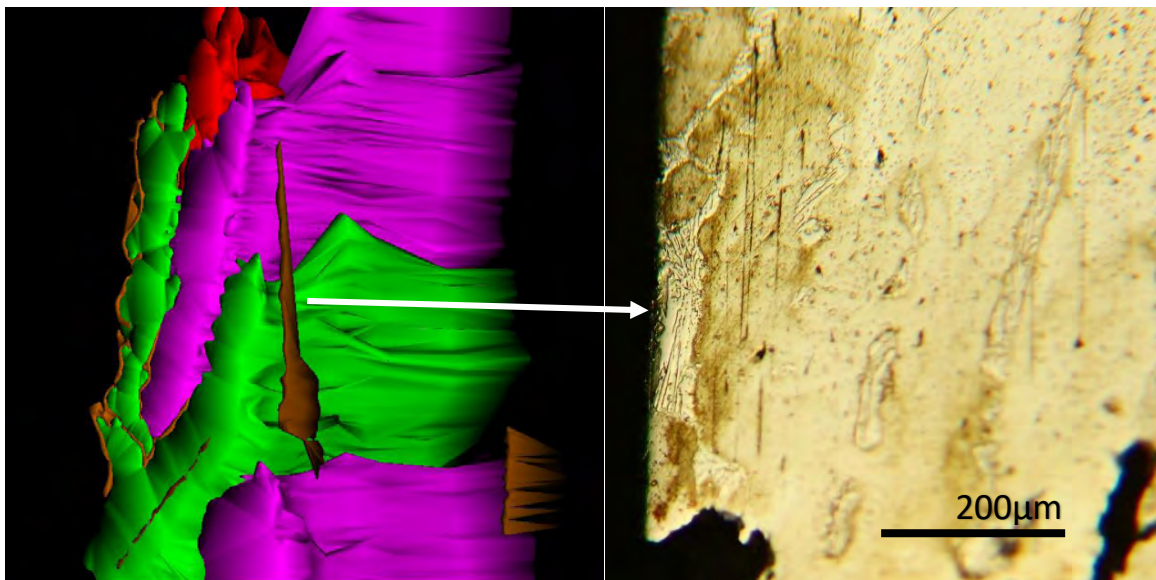
*Figure 3-14 3D model of cracks combined with carbide network*

Figure 3.13 and 3.14 represent the spatial evolution the of cracks. Their evolvement in space, looks very similar with the dendritic pattern that carbide network follows. Also, there is a constant observation of the relation between carbides and cracks. It seems like cracks end up to a carbide and that carbides are sometimes the only odd between cracks.

A 3D display of the real microstructure has also been conducted. This method employs two perpendicular metallographies that after merging, create a 3D projection (Figure 3.15) which allows the comparison with the 3D model of the software. Moreover, the side view as provided by the 3D model coincides with the findings from metallography as demonstrated in Figure 3.16, in relation to the primary carbides. Actually, Figure 3.16 b depicts a section view of a carbide which thickness is 50μm and height of 200μm.



*Figure 3-15 A common way to reproduce quickly and easily a 3D view and in this case is used to compare results with the software output. It is quite impressive the evolvement of the crack*



*Figure 3-16 Comparison of 3D model with metallography (side view).*

Figure 3.17 provides a comparison regarding the morphology of the primary carbides. The 3D model representation is very close to the results reported in the literature [15].

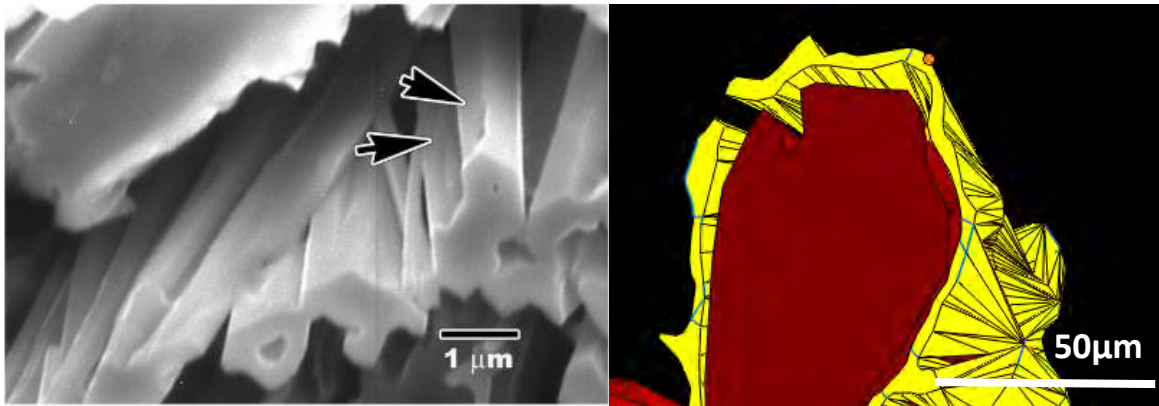


Figure 3-17 (a) Rod like eutectic M7C3 carbides (b) 3D model reconstruction of M7C3 carbides

Furthermore, the software provides the ability of volumetric fraction measurement. Figure 3.15 shows the results of volume calculation and Figure 3.16 presents the volume fraction calculation.

Object	Start	End	Count	Surface area	Flat area	Volume
carvidio1	4	8	9	11.2379	0.862641	0.284232
carvidio10	1	2	2	7.16417	0.192712	0.192712
carvidio11	6	8	3	2.7044	0.306111	0.0765278
carvidio2	1	8	8	56.2067	1.95737	1.1851
carvidio4	1	8	10	55.9463	1.84117	1.06621
carvidio5	3	7	6	12.6408	0.829675	0.415788
carvidio6	1	8	8	14.8868	0.394199	0.275588
carvidio7	1	5	5	4.89163	0.144584	0.117798
carvidio8	1	4	4	31.8654	0.762346	0.675786
carvidio9	1	8	8	21.2886	0.731185	0.435018
deksia	1	8	8	33.6795	14.3296	8.07015
kokkinos	1	5	5	10.9045	1.40662	1.23433
kokkinos_kok	1	8	8	43.7849	12.968	9.04694
megalos	1	8	8	81.1437	27.7411	18.492
megalosdeksia	1	8	8	79.9252	65.6412	39.0052
prasino_dendr	1	8	11	64.6334	24.0373	11.9959
prasinos_kok...	1	8	8	31.3541	9.61478	4.11589

Figure 3-18 Volumetric measurements

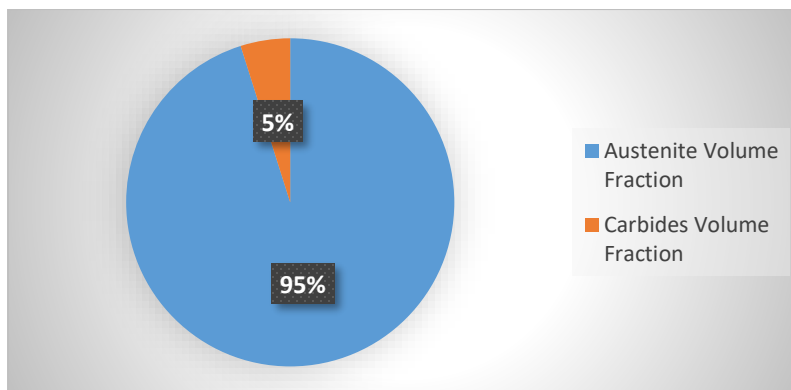


Figure 3-19 The volume fraction calculation from software. 95% Austenite and 5% Carbides

Below (Figure 3.20 and Figure 3.12 present microhardness measurements at carbides that were illustrated in the 3D model. This could be beneficial for characterization of the carbides, if the distinguish could be accomplished only with the microhardness value available.

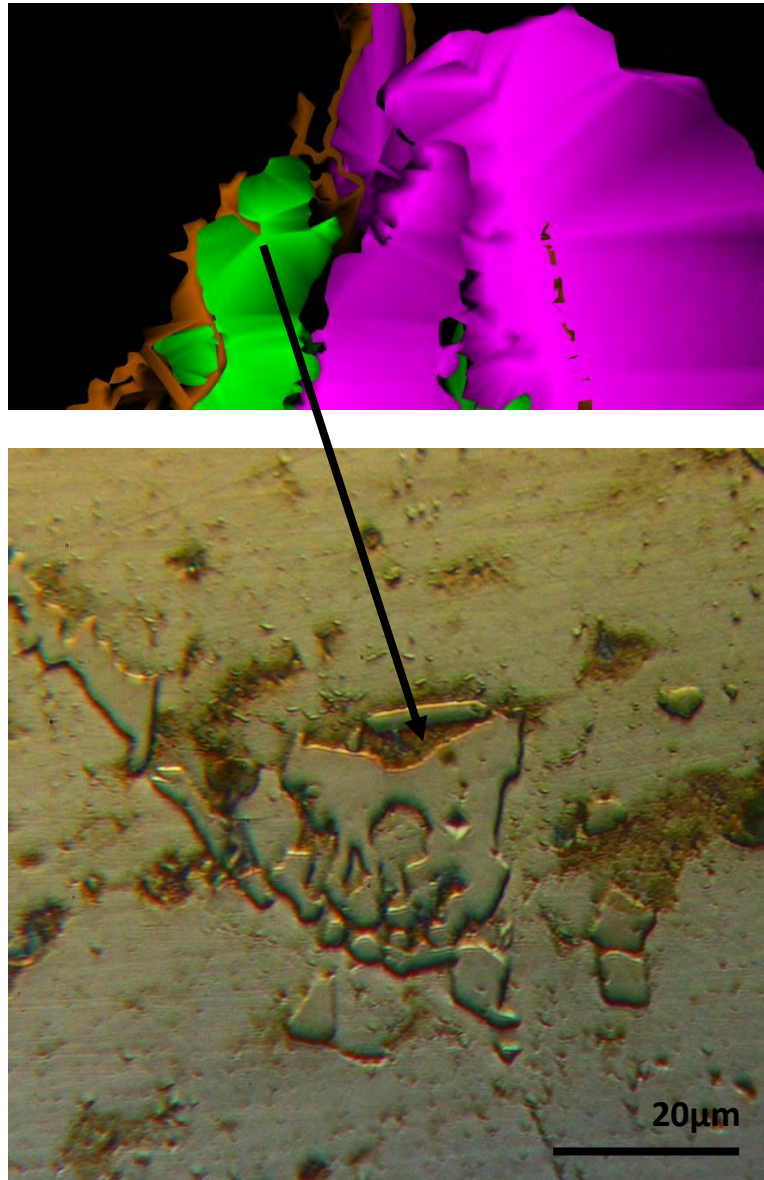


Figure 3-20 Microhardness measurement at carbide that was illustrated in 3D model. 1530  $HV_{0.01}$

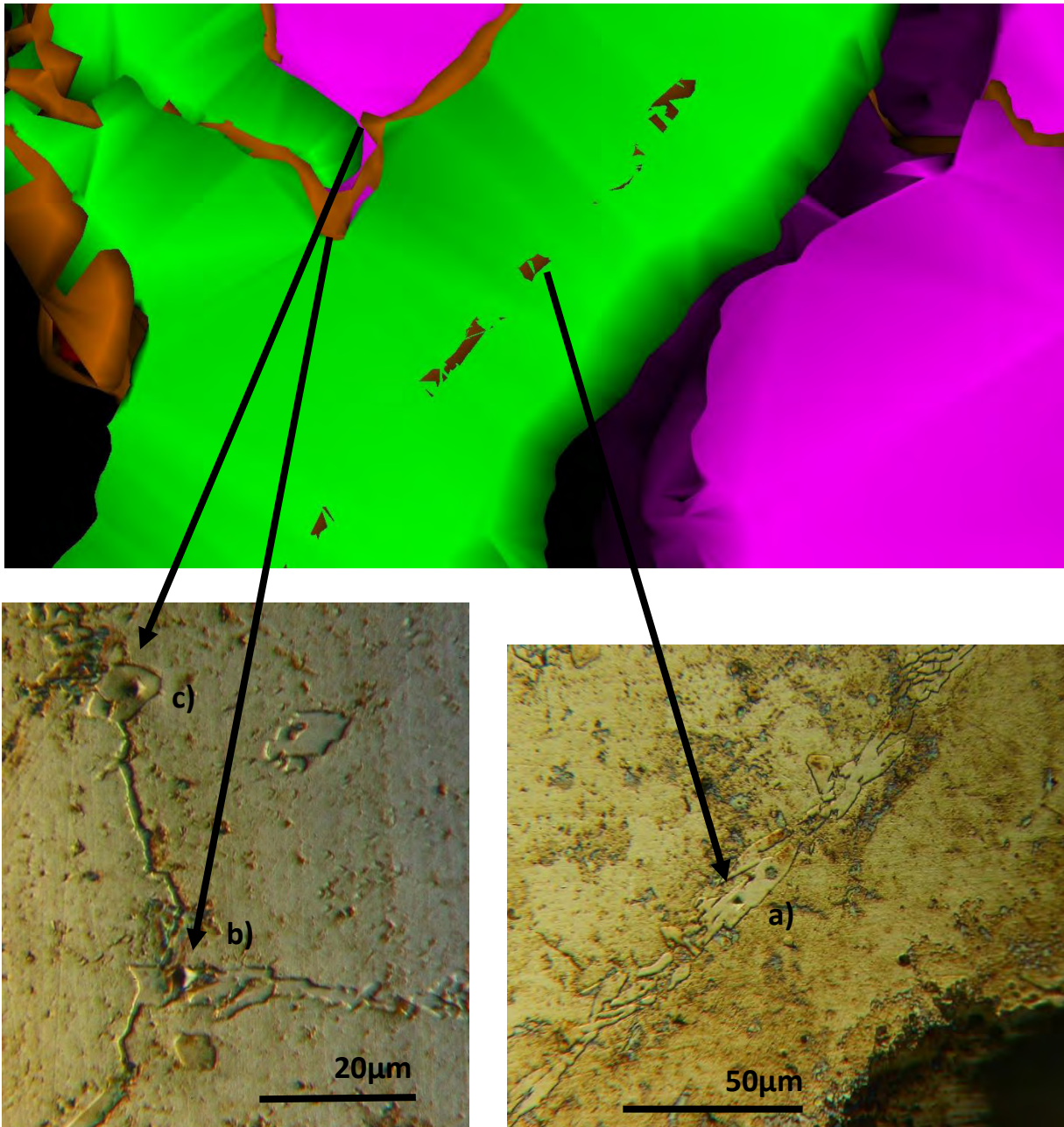


Figure 3-21 Microhardness measurement at carbides that were illustrated in 3D model. a) 1600 HV0.01 b) 1080 HV0.01

### 3.3 SEM/EDS Analyses

The 3D model on its own is not able to provide completed metallurgical information. But this can be accomplished with a combination of experimental procedures such as SEM/EDS as well as microhardness tests (3.4). SEM combined with EDS were performed to characterize the carbides and to enrich the study and are presented below.

The aim of SEM/EDS is to provide information that will assist to distinguish the phases and mainly the carbides. The phases that constitute the microstructure are austenitic matrix,  $M_{23}C_6$ , MC and  $M_7C_3$ .

The Nb rich regions appear as white phase in SEM images, due to the difference in atomic weight between Nb and Cr-rich (Figure 3.22).

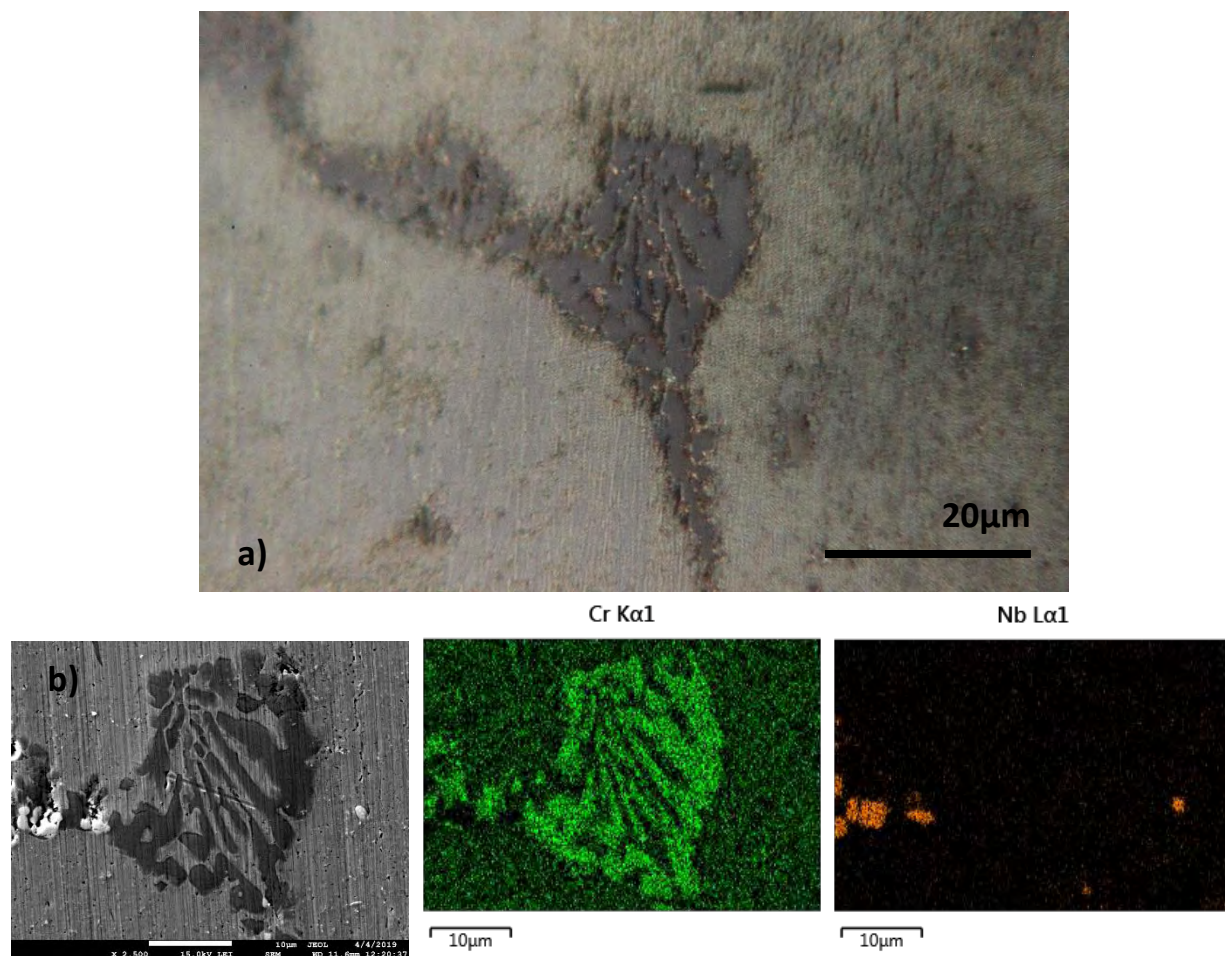
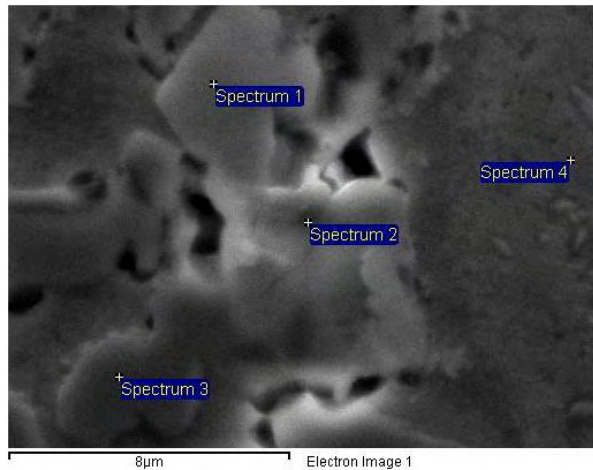


Figure 3-22 a) Optical microscope capture of the carbide b) The X-ray map of the same carbide indicates that white region at the left of the carbide is Nb carbide and the carbide in the middle of the image is Cr-rich carbide

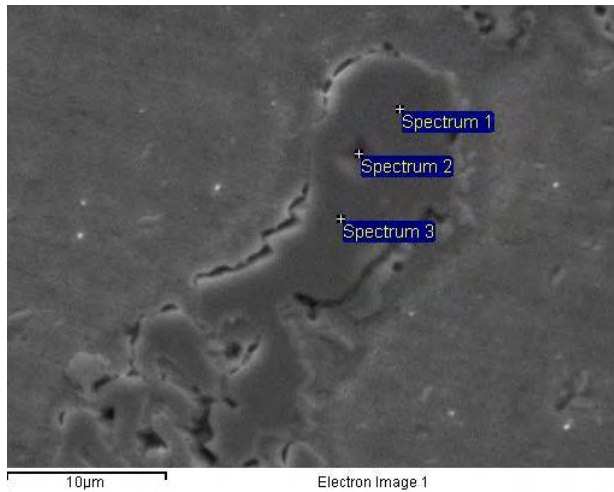
However, the most difficult task of the characterization process was the identification between  $M_7C_3$  and  $M_{23}C_6$ . As previously mentioned, literature reports that Cr-map show no significant differences between the two carbides. Yet,  $M_{23}C_6$  probably contains more Fe, Ni. Below, the relevant results are presented in Figures 3.23 – 3.27.



Spectrum	In stats.	C	Si	Cr	Fe	Ni	Nb	Mo	Total
Spectrum 1	Yes	14.19	0.07	2.94	0.86	1.19	80.75		100.00
Spectrum 2	Yes	18.50	0.00	2.83	0.86	1.13	76.67		100.00
Spectrum 3	Yes	20.53		52.72	15.88	10.54		0.33	100.00
Spectrum 4	Yes	11.28	1.50	23.13	35.20	28.68		0.22	100.00
Max.		20.53	1.50	52.72	35.20	28.68	80.75	0.33	
Min.		11.28	0.00	2.83	0.86	1.13	76.67	0.22	

All results in weight%

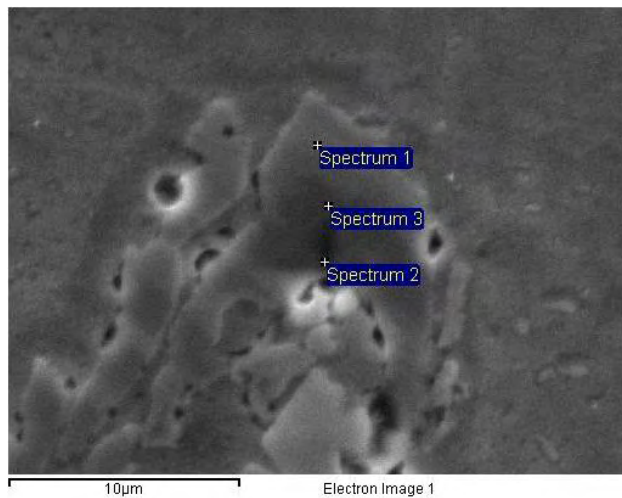
Figure 3-23 Spectrum 3, denotes M23C6 carbide. Spectrum 1 and 2 denote MC carbide



Spectrum	In stats.	C	Si	Cr	Fe	Ni	Nb	Mo	Total
Spectrum 1	Yes	18.97	0.21	70.32	9.31	0.71	0.02	0.47	100.00
Spectrum 2	Yes	16.00	0.50	73.38	8.27	1.21	0.54	0.09	100.00
Spectrum 3	Yes	18.98	0.09	70.66	7.80	1.91	0.41	0.16	100.00
Mean		17.98	0.27	71.45	8.46	1.28	0.32	0.24	100.00
Std. deviation		1.72	0.21	1.68	0.78	0.60	0.27	0.20	
Max.		18.98	0.50	73.38	9.31	1.91	0.54	0.47	
Min.		16.00	0.09	70.32	7.80	0.71	0.02	0.09	

All results in weight%

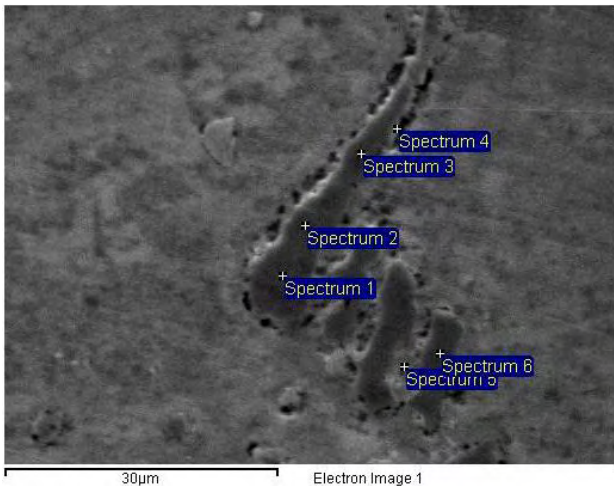
Figure 3-24 Spectrum 1, 2 and 3 indicate composition M7C3.



Spectrum	In stats.	C	Si	Cr	Fe	Ni	Nb	Mo	Total
Spectrum 1	Yes	20.88	0.57	52.88	16.67	8.04	0.71	0.24	100.00
Spectrum 2	Yes	14.12	0.22	69.82	12.37	2.99	0.47		100.00
Spectrum 3	Yes	18.80	0.42	68.70	7.47	1.50	1.28	1.82	100.00
Max.		20.88	0.57	69.82	16.67	8.04	1.28	1.82	
Min.		14.12	0.22	52.88	7.47	1.50	0.47	0.24	

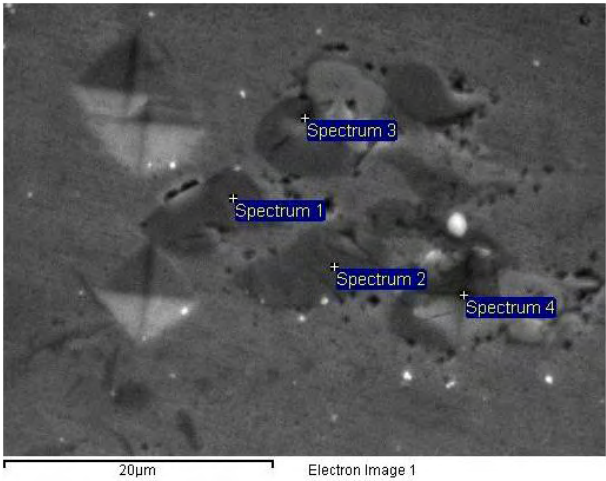
All results in weight%

Figure 3-25 Spectrum 1 corresponds to M23C6 and Spectrum 3 to M7C3. This result confirms the literature reports about M7C3 transformation.



Spectrum	In stats.	C	Si	Cr	Fe	Ni	Nb	Mo	Total
Spectrum 1	Yes	17.20	0.41	71.68	8.56	0.84	0.73	0.58	100.00
Spectrum 2	Yes	18.18		72.61	7.80	1.42			100.00
Spectrum 3	Yes	14.54		73.88	9.67	1.92			100.00
Spectrum 4	Yes	27.19	0.40	54.92	11.55	5.66	0.27		100.00
Spectrum 5	Yes	18.76	2.16	16.59	34.48	28.01			100.00
Spectrum 6	Yes	17.40	0.07	73.40	7.48	1.28	0.36	0.01	100.00
Max.		27.19	2.16	73.88	34.48	28.01	0.73	0.58	
Min.		14.54	0.07	16.59	7.48	0.84	0.27	0.01	

Figure 3-26 Spectrum 1,2,3 and 6 indicates M7C3 stoichiometry



Spectrum	In stats.	C	Si	Cr	Fe	Ni	Nb	Mo	Total
Spectrum 1	Yes	11.63		80.51	5.22	0.94	1.71		100.00
Spectrum 2	Yes	17.38	0.15	75.71	4.62	0.10	1.79	0.25	100.00
Spectrum 3	Yes	13.21		76.49	4.03	1.24	3.71	1.32	100.00
Spectrum 4	Yes	13.27	0.40	78.08	5.78	1.05	1.27	0.14	100.00
Max.		17.38	0.40	80.51	5.78	1.24	3.71	1.32	
Min.		11.63	0.15	75.71	4.03	0.10	1.27	0.14	

All results in weight%

Figure 3-27 Spectrum 1,2,3 correspond to M7C3 composition

### 3.4 Microhardness Measurements

Microhardness measurements had been conducted at the carbide network. A force load of 10gr had been selected in order to minimize the size of the imprints. Representative measurements are marked in Fig. 3.28 as 1-12, and the microhardness values are depicted in Table 3.1. Very high values ranging from 413 HV<sub>0.01</sub> up to 1644 HV<sub>0.01</sub> were measured. An exception stands for the T5 where the imprint was partially shared between the carbide and the austenite matrix.

Typical microhardness values reported in the literature is provided in Figure 3.29 [16], are in good agreement with the above findings.

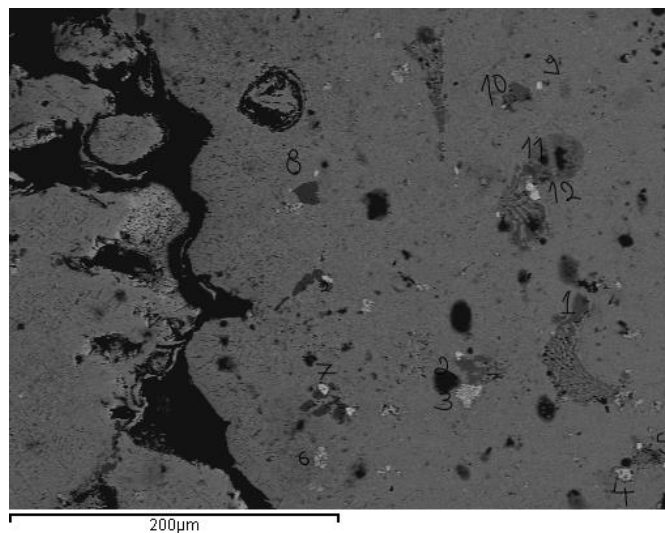


Figure 3-28 The guide shows the number and the position of each measurement

Table 3-1 Microhardness values.

	Measurement 1 (HV <sub>0.01</sub> )	Measurement 2 (HV <sub>0.01</sub> )	Color of Region
T1	1431	1488	Black
T2	1410	1340	Black
T3	790	752	White
T4	688	741	White
T5	263	255	Black
T6	580	536	White
T7	993	1219	Black
T8	1327	1102	Black
T9	413	466	White
T10	1712	1644	Black
T11	785	775	Black
T12	890	910	White

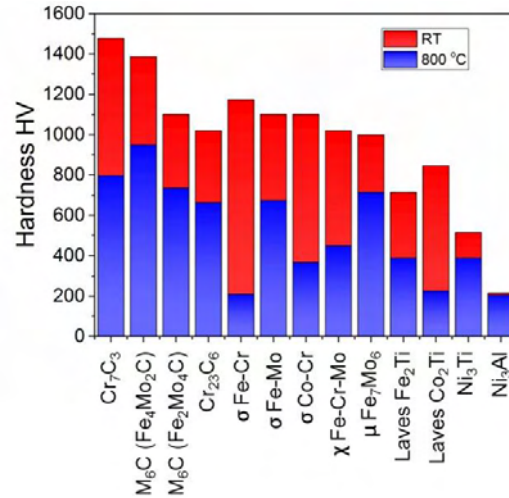


Figure 3-29 The relative values suggest that Cr<sub>7</sub>C<sub>3</sub> has higher hardness than Cr<sub>23</sub>C<sub>6</sub>.

The results are presented in Figure 3.28, where it is demonstrated that the Cr-rich carbides exhibit higher hardness in relation to the NbC. The range of hardness values for NbC is 439-900 HV<sub>0.01</sub> while the Cr-rich 775-1678 HV<sub>0.01</sub>. Also, there are three hardness results that are combined with EDS analysis. Two of them are identified as M<sub>7</sub>C<sub>3</sub> with hardness 1219 and 1459 HV<sub>0.01</sub>. The other one is identified as M<sub>23</sub>C<sub>6</sub> with hardness 775 HV<sub>0.01</sub>.

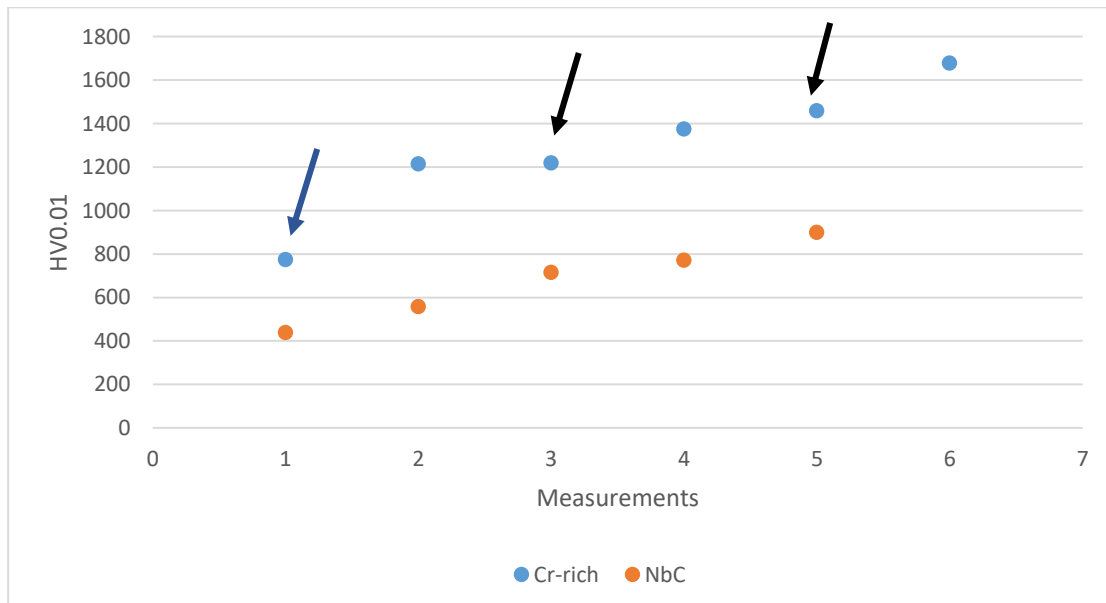


Figure 3-30 The black arrows indicate measurements at characterized carbides as M<sub>7</sub>C<sub>3</sub>. Blue arrow indicates a measurement which corresponds at M<sub>23</sub>C<sub>6</sub> carbide

## Chapter 4- Computational Simulation

Within this work, it has been decided that a computation approach would provide a more integrated aspect of the study and would enrich the metallurgical content of the project. So, some primary calculations implemented. It had not been attempted a sophisticated approach with plenty results because this was not the purpose of that Chapter. For that reason, more fundamental diagrams had been tried, that provide the right initial tools for our study. This procedure Scheil diagram and coarsening simulation. The thermodynamic software that had been used is Thermocalc.

### 4.1 Scheil-Gulliver Simulation

A short preview of Scheil methodology shows that it describes a non-equilibrium solidification under assumptions. These are no diffusion in solid state, infinite mixing in liquid and equilibrium condition at solid-liquid interface. These assumptions describe a quite fast cooling. In fact, Scheil diagram shows in which sequence the phases are formed during the solidification process. At that point it should be mentioned that this technique does not predict the amount of every solidified phase. To set up the model in Thermocalc, the composition is needed. Table 4.3 shows the composition that had been input. The fact that there are four missing elements compared to the actual composition, means that the output might be inaccurate but not incorrect (as the missing elements have small concentration and supplementary role).

An advanced option of the calculator is the selection “Global Minimization” which is recommended at Thermocalc user’s guide. This option activates a mathematical tool of optimization which finds the global minima/maxima of a function. Both cases had been carried out, as the plot of this calculation is fast. Figure 4.1 presents the case of Scheil with the option “Global Minimization” activated and Figure 4.2 presents the diagram with the option deactivated.

*Table 4-1 Mn and Si are missing. When Scheil simulation attempted with the bulk chemical composition the output was not reasonable, so it had been decided to simplified, by keeping only the crucial elements*

C	Cr	Ni	Nb	Fe
0.4	25	35	1.2	38.4

The sequence with “Global Minimization” on is:

Liquid → Liquid+Austenite → Liquid+Austenite+M<sub>7</sub>C<sub>3</sub> → Liquid+Austenite+M<sub>7</sub>C<sub>3</sub>+MC →  
Liquid+Austenite+M<sub>7</sub>C<sub>3</sub>+MC+M<sub>23</sub>C<sub>6</sub>

The sequence with “Global Minimization” off is:

Liquid → Liquid+Austenite → Liquid+Austenite+M<sub>7</sub>C<sub>3</sub> → Liquid+Austenite+M<sub>7</sub>C<sub>3</sub>+M<sub>23</sub>C<sub>6</sub> →  
Liquid+Austenite+M<sub>7</sub>C<sub>3</sub>+MC

The first observation is the starting and ending temperatures. The starting temperature is 1370 °C and is common for both diagrams. However, there is significant difference at the final temperature, which is 1250 °C and 1000 °C at Figure 4.1 and Figure 4.2 respectively.

The two diagrams do not recommend the same solidified composition of phases. The difference lies on the appearance of  $M_{23}C_6$  or not, which means that Austenite,  $M_7C_3$  and MC are commonly predicted from both simulations. Moreover, the final composition of Figure 4.1 solidification diagram is formed at 90% of the solidification process while final composition of Figure 4.2 solidification diagram is formed at 97% of the process.

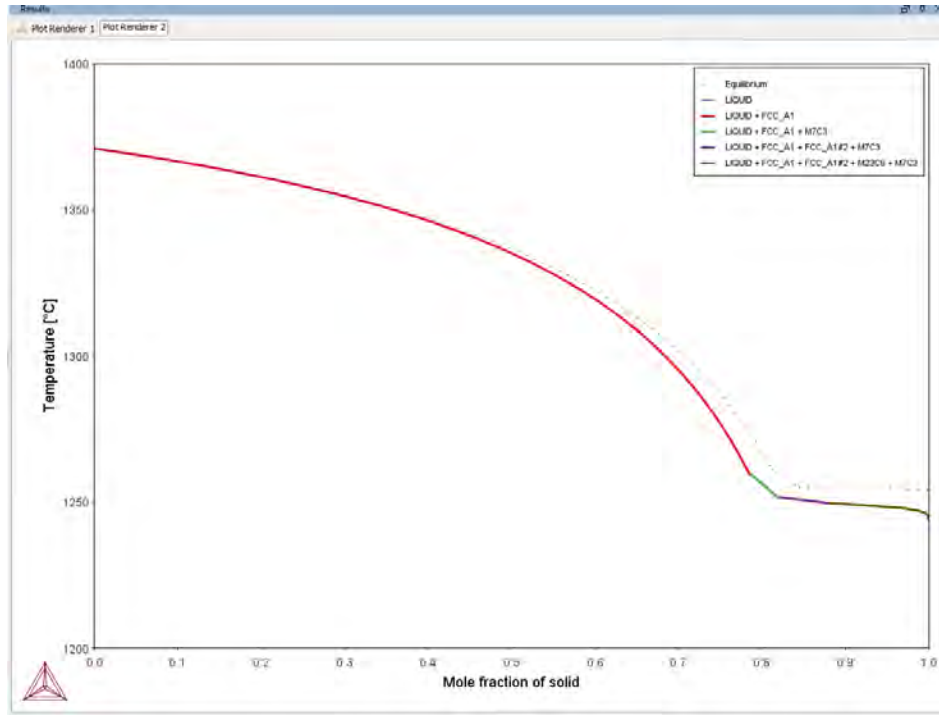


Figure 4-1 The Scheil-Gulliver diagram with “Global Minimization” indicates solidification sequence Austenite,  $M_7C_3$ , MC,  $M_{23}C_6$ . The dotted line is the equilibrium line which is the solidification according to phase diagram

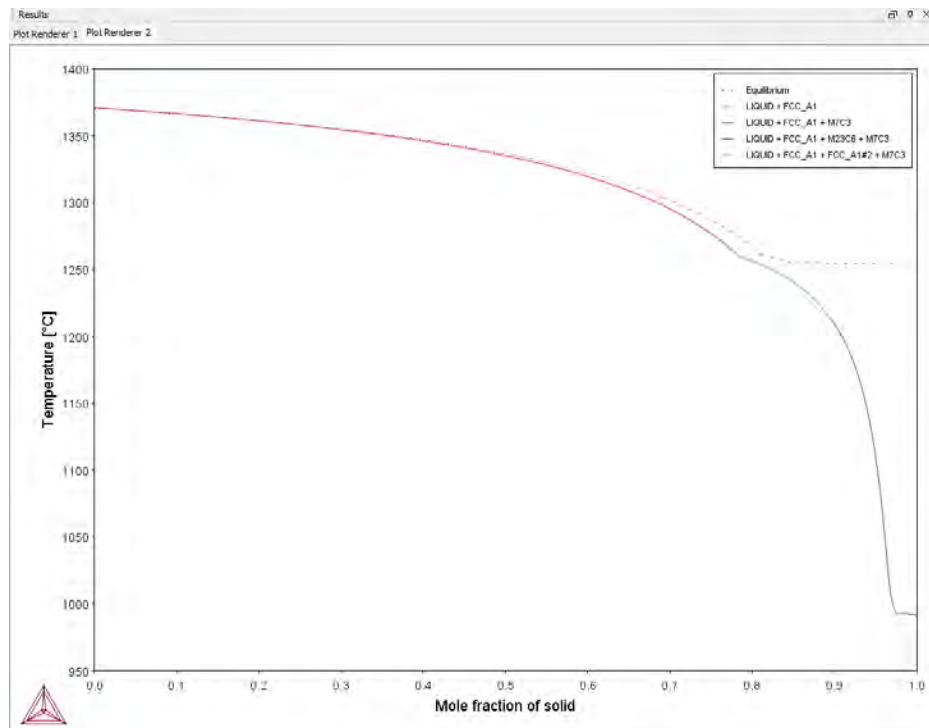


Figure 4-2 The Scheil-Gulliver diagram without "Global Minimization" indicates solidification sequence Austenite, M7C3, M23C6, MC.



## Chapter 5 - Discussion and Conclusions

### 5.1 Discussion

In this Chapter, the data from experimental part, literature sources and computational approach, are collected combined and compared in order to capitalize the work.

Starting from volume fraction estimation according to data from Figure 2.10 and Figure 3.19. Figure 2.10 recommends that the total carbide volume fraction is about 10%. Figure 3.19 supports that the total carbide volume fraction is almost 5%. As a consequence, the results from the 3D model with these from literature, present difference.

Then, the phases existing in the as cast condition exhibits a diversity of results. For example, [18] indicates that the as cast microstructure is consisted of Austenite,  $M_7C_3$ ,  $M_{23}C_6$  and MC, while [7] indicates that as cast is consisted of Austenite,  $M_7C_3$  and MC. In addition, Figure 4.1 and Figure 4.2 create the same contradiction. Therefore, the results of solidification simulation vary in the same way that vary in literature sources.

One more comparison is the one between literature and computational results about the solidification sequence. [7]

predicts Liquid  $\rightarrow$  Liquid+Austenite  $\rightarrow$  Liquid+Austenite+MC  $\rightarrow$  Liquid+Austenite+ $M_7C_3$ +MC.

Scheil model predicts

Liquid  $\rightarrow$  Liquid+Austenite  $\rightarrow$  Liquid+Austenite+ $M_7C_3$   $\rightarrow$  Liquid+Austenite+ $M_7C_3$ + $M_{23}C_6$   $\rightarrow$  Liquid+Austenite+ $M_7C_3$ +MC. The significant difference is that MC is solidified firstly, according to literature source. On the other hand, Scheil simulation indicates that  $M_7C_3$  is solidified first. At this point it should be mentioned that phase diagram indicates that  $M_7C_3$  is the first solidified carbide, at carbon content over 0.2 wt.%.

Another fact that can be discussed, is the hardness of carbides. There are data from literature and from the microhardness measurements that conducted as part of the experimental study. More specifically, [16] and Figure 3.29 indicates that hardness of  $Cr_7C_3$  carbide is around 1400-1500 HV at RT and for  $Cr_{23}C_6$  the hardness is around 1000 HV. The combined data from EDS and microhardness that are presented in Figure 3.30, suggest that  $M_7C_3$  microhardness varies from 1200 to 1400 HV0.01. Given that the Figure 3.29 is referred at  $Cr_7C_3$  and not at  $M_7C_3$ , it should be noted that the results are quite close. The microhardness of  $M_{23}C_6$  according to Figure 3.30 is 780 HV0.01, which is not far from 1000 HV.

It is also worth mentioned the quality of 3D model and its consequences. It seems that creates an accepted output, as it hasn't ignored any crucial feature.

## 5.2 Conclusion

To conclude:

- 3D model and observations for microstructure:
  - Austenite is in a form of a whole dendrite
  - Carbide network consisted from many carbides, supporting as a frame the austenite matrix
  - Inter-dendritic carbides penetrate the matrix
  - Carbide pattern like solid thin film around matrix but sometimes is discontinuous and has gaps
  - Complicated and multidimensional network with significant depth that extend in the whole tube high
  - Secondary precipitates exhibit low thickness compared to primary
  - Creep cracks evolve in parallel to the primary carbide network.
- Volume fraction
  - Literature: 10% carbides
  - 3D model: 6% carbides
- As cast composition
  - Literature: Austenite,  $M_7C_3$  and MC/ Austenite,  $M_7C_3$ ,  $M_{23}C_6$  and MC
  - Thermocalc: Austenite,  $M_7C_3$  and MC/ Austenite,  $M_7C_3$ ,  $M_{23}C_6$  and MC
- Solidification sequence
  - Literature: First formed carbide MC
  - Thermocalc: First formed carbide  $M_7C_3$
- Carbide's Hardness:
  - Literature:  $Cr_7C_3$  1400-1500 HV and  $Cr_{23}C_6$  1000 HV
  - Experiment:  $M_7C_3$  1200 to 1400 HV0.01 and  $M_{23}C_6$  780 HV0.01
- $M_7C_3$  to  $M_{23}C_6$  transformation
  - Literature:  $M_{23}C_6$  like cell around  $M_7C_3$  nucleus
  - Experiment:  $M_{23}C_6$  above  $M_7C_3$

## Chapter 6- Future Work

- Further research can be conducted on the 3D representation of the voids within the microstructure
- XCT can be conducted and compared with the current method
- The same method could be applied at low height and oriented to very fine resolution.
- A different 3D software could be used to create the model. A more recent tool might be quicker and with even better result.
- Furthermore, a more extended study between SEM/EDS and microhardness could be done, in order to create a guide that will allow carbide characterization based on hardness values.
- Moreover, a more complete and extended simulation at all the metallurgical phenomena that take place in the microstructure, could be done



## Chapter 7 - Bibliography

- [1] <https://www.ammoniaknowhow.com/fiorda-case-study-failure-of-reformer-tubes-at-ammonia-plant/>
- [2] <https://www.slideshare.net/GerardBHawkins/reformer-tube-metallurgy-design-considerations-failure-mechanisms-inspection-methods>
- [3] Gregory N. Haidemenopoulos. Physical Metallurgy. Tziolas Publications, 2007.
- [4] Mike Reichelt, Lydia Joubert, John Perrino, Ai Leen Koh, Ibanri Phanwar, Ann M. Arvin. 3D Reconstruction of VZV Infected Cell Nuclei and PML Nuclear Cages by Serial Section Array Scanning Electron Microscopy and Electron Tomography. PLoS Pathog 8(6): e1002740. doi:10.1371/journal.ppat.1002740.
- [5] J.T. Benzing, A. Kwiatkowski da Silva, L. Morsdorf, J. Bentley, D. Ponge, A. Dutta, J. Han, J.R. McBride, B. Van Leer, B. Gault, D. Raabe, J.E. Wittig. Multi-scale characterization of austenite reversion and martensite recovery in a cold-rolled medium-Mn steel. Acta Materialia 166 (2019) 512e530
- [6] Gianni Nicoletto, Giancarlo Anzelottiand, Radomila Konečná. X-ray Computed Tomography vs. Metallography for Pore Sizing and Fatigue of Cast Al-alloys. Procedia Engineering 2 (2010) 547–554.
- [7] Minshi Wang, Dominique Flahaut, Zhu Zhang, Ian P. Jones, Yu Lung Chiu. Primary carbide transformation in a high performance micro-alloy at 1000 °C. Journal of Alloys and Compounds 781 (2019) 751e760.
- [8] Mahyar Mohammadnezhad, Vahid Javaheri, Morteza Shamanian, Shahram Rizaneh, Jerzy A. Szpunar. INSIGHT TO THE MICROSTRUCTURE CHARACTERIZATION OF A HP AUSTENITIC HEAT RESISTANT STEEL AFTER LONG-TERM SERVICE EXPOSURE. Acta Metallurgica Slovakian, Vol. 24, 2018, No. 4, p. 296-305.
- [9] Luiz Henrique de Almeida, André Freitas Ribeiro, Iain Le Maya. Microstructural characterization of modified 25Cr–35Ni centrifugally cast steel furnace tubes. Materials Characterization 49 (2003) 219 – 229.
- [10] Majid Abbasi, Ihho Park, Yunjo Ro, Youngsu Ji, Raghavan Ayer, Jae-Hyeok Shim. G-phase formation in twenty-years aged heat-resistant cast austenitic steel reformer tube. Materials Characterization 148 (2019) 297–306.

- [11] A.D. Zervaki, H. Kamoutsi, S.I. Alkhoori, S. Jaffar, K. Polychronopoulou, G.N. Haidemenopoulos. Metallographic assessment of creep in cast tubes of heat resistant steels. ICEAF V5th International Conference of Engineering Against Failure 20 - 22 June 2018 - Chios Island, Greece.
- [12] G. N. Haidemenopoulos, K. Polychronopoulou, A. D. Zervaki, H. Kamoutsi, S. I. Alkhoori, S. Jaffar, P. Cho and H. Mavros. Aging Phenomena during In-Service Creep Exposure of Heat-Resistant Steels. *Metals* 2019, 9, 800.
- [13] Natalie C. de Siqueira, Monica P. Arenas, Priscila D. de Almeida, Leonardo S. Araújo, Carlos B. Eckstein, Laudemiro Nogueira Jr, Luiz H. de Almeida, Gabriela R. Pereira. Characterization of the aging state of modified HP steels by ultrasonic signal processing and the effect of creep voids in the interdendritic region. *jmatrrestechol.* 2018:7(3):361–365.
- [14] <http://synapses.bu.edu/tools/>
- [15] A. Bedolla-Jacuinde, B. Hernández, L. Béjar-Gómez. SEM study on the  $M_7C_3$  carbide nucleation during eutectic solidification of high-chromium white irons. *Z. Metallkd.* 96 (2005) 12.
- [16] J.H. Westbrook. Temperature dependence of the hardness of secondary phases common in turbine bucket alloys. *J. Met.*, 9 (1957), pp. 898-904.
- [17] [http://steel.ndsl.kr/htm/HR\\_Steels.htm](http://steel.ndsl.kr/htm/HR_Steels.htm)
- [18] C.J. Liu, Y. Chen. Variations of the microstructure and mechanical properties of HP40Nb hydrogen reformer tube with time at elevated temperature. *Materials and Design* 32 (2011) 2507–2512.
- [19] Damir Hodžid, Ismar Hajro, 2007. Assessment of microstructure degradation of creep exposed boiler steels. *11th International Research/Expert Conference*, September 05-09 2007